Spurious Diapycnal Mixing Associated with Advection in a *z*-Coordinate Ocean Model

STEPHEN M. GRIFFIES, RONALD C. PACANOWSKI, AND ROBERT W. HALLBERG

NOAA/Geophysical Fluid Dynamics Laboratory, Princeton, New Jersey

(Manuscript received 26 October 1998, in final form 22 February 1999)

ABSTRACT

This paper discusses spurious diapycnal mixing associated with the transport of density in a *z*-coordinate ocean model. A general method, based on the work of Winters and collaborators, is employed for empirically diagnosing an effective diapycnal diffusivity corresponding to any numerical transport process. This method is then used to quantify the spurious mixing engendered by various numerical representations of advection. Both coarse and fine resolution examples are provided that illustrate the importance of adequately resolving the admitted scales of motion in order to maintain a small amount of mixing consistent with that measured within the ocean's pycnocline. Such resolution depends on details of the advection scheme, momentum and tracer dissipation, and grid resolution. Vertical transport processes, such as convective adjustment, act as yet another means to increase the spurious mixing introduced by dispersive errors from numerical advective fluxes.

1. Introduction

There are many physical processes that mix density in the ocean. Breaking internal waves, convective overturning, salt fingering, diffusive interleaving, molecular diffusion, cabbeling, and thermobaricity are some examples (for reviews see, e.g., Gregg 1987; Large et al. 1994). Such mixing results in an irreversible transfer of water mass properties across neutral surfaces, thus transforming the water masses themselves. Measurements indicate that the level of mixing occurring across the pycnocline in certain parts of the ocean is quite small (Rooth and Östlund 1972; Veronis 1975, 1977; Ledwell et al. 1993; Toole et al. 1994; Kunze and Sanford 1996). Indeed, in some regions, the mixing appears to be minimal all the way to the abyss (Kunze and Sanford 1996). There are notable exceptions associated with enhanced mixing in regions above rough topography (Polzin et al. 1997), in shallow basins (Ledwell et al. 1991), and near seamounts (Toole et al. 1997).

In contrast to the irreversible mixing processes, advection of density leads only to the reversible stirring or interchange of the fluid parcels' density [Eckart (1948) provides some intuitive examples of the difference between stirring and mixing]. For this reason, advection is said to be an *adiabatic* transport process.

The adiabatic property of advection is difficult to maintain in a numerical model of stratified flow unless it is explicitly built into the model's algorithmic framework. Such is the basis of isopycnal layer models (e.g., Bleck et al. 1992; Oberhuber 1993; Hallberg 1995). By construction, these models preserve a predefined number of potential density classes, and these classes are mixed only through the explicit introduction of irreversible processes. Consequently, within the confines of the chosen classes, the models respect the adiabatic property. Geopotential level models (*z*-models (e.g., Pacanowski and Griffies 1999; Marshall et al. 1997) and sigma-coordinate models (e.g., Blumberg and Mellor 1987; Haidvogel et al. 1991) instead rely on numerical convergence to approximate adiabaticity. A question that arises is whether numerical convergence is sufficient to maintain a physically small amount of irreversible mixing in the level and sigma coordinate models.

Since the work of F. Bryan (1987), it has been known that ocean model dynamics are quite sensitive to the amount of diapycnal mixing. Recent work by Marotzke (1997), Toggweiler and Samuels (1998), Huang (1998, 1999), Samelson and Vallis (1997), Hirst and McDougall (1998), and Park and Bryan (2000) highlight some of the climatologically related issues. Of particular note, we emphasize that the recent study of Hallberg (1999, unpublished manuscript) indicates that a global isopycnal model starting from an unstratified state and using a diapycnal diffusivity of 0.1 $cm^2\ s^{-1}$ in the pycnocline region, a number consistent with recent measurements, is able to largely reproduce the water mass distributions seen in the Levitus atlas (Levitus 1982). This result is consistent with the suggestions of Toggweiler and Samuels, who emphasize the importance of the Southern Ocean for setting the thermocline depth throughout the World Ocean. In general,

Corresponding author address: Dr. S. Griffies, Geophysical Fluid Dynamics Laboratory, Route 1, P.O. Box 308, Forrestal Campus, Princeton, NJ 08542.
E-mail: smg@gfdl.gov

models using larger pycnocline diffusivities become too ''diffuse,'' which can result in a loss of physical integrity. A conclusion from comparing the measurements and model results is that it is vital to maintain control over the amount of mixing in ocean models.

Unfortunately, there are numerous opportunities in level and sigma coordinate models to spuriously add to the effective mixing. Two examples from a *z*-model were discussed by Griffies et al. (1998) and Griffies (1998), and the new approaches outlined there significantly reduce the spurious mixing of density classes. Indeed, the new isoneutral diffusion scheme of Griffies et al. (1998) eliminates, by construction, such mixing to machine accuracy. In the present paper, focus is given to the numerical representation of advective transport of tracers, in particular density.

The fundamental problem with numerically representing tracer advection is the need to trade off between respecting conservation of the tracer's second moment and maintaining smoothness. On one hand, dispersion errors from second moment conserving advection schemes (e.g., centered differences) permit the development of extrema in the tracer field whose values may lie outside those that are physically realistic. When coupled to dynamics through the pressure field, extrema in density introduce unphysical sources of gravity waves. More dramatically, they often introduce statically unstable profiles, which are then irreversibly homogenized by rapidly acting vertical processes (i.e., convective adjustment). In contrast to the centered schemes, simple monotonic advection schemes (e.g., upwind advection) generally add a nontrivial amount of irreversible ''numerical diffusion'' (e.g., Molenkamp 1968). More sophisticated schemes, such as flux corrected transport (FCT) (Boris and Book 1973; Zalesak 1979; Gerdes et al. 1991), aim to balance the trade-off while maintaining certain desirable properties such as monotonicity.

The purpose of this paper is to empirically quantify the rate of spurious diapycnal mixing associated with numerical advection for some idealized model configurations. The method used for this purpose relies on the work of Winters et al. (1995) and Winters and D'Asaro (1996). Their framework provides for the diagnosis of an effective diapycnal diffusivity, which permits a comparison between the spurious mixing associated with numerical advection to the mixing inferred from ocean measurements.

The remainder of this paper consists of the following sections. Section 2 briefly summarizes the advection schemes considered in this paper. Section 3 presents a one-dimensional seasonally forced thermocline model, which illustrates the coupling of vertical convection to advection. Section 4 discusses the theoretical framework used to diagnose effective diapycnal mixing coefficients associated with model transport processes. Section 5 diagnoses the effective mixing appearing in a coarse-resolution sector model. It is found that to ensure a physically acceptable amount of spurious mixing, the grid must adequately resolve the scales of motion; most notably, the western boundary current. What resolution qualifies as ''adequate'' is exemplified. Section 6 performs the same diagnosis for an eddy-permitting midlatitude channel model. Analysis of a number of experiments reveals the nontrivial nature of simultaneously resolving the dominant flow features, dissipating the variance cascade, and keeping the level of spurious diapycnal mixing low. Section 7 finishes the paper with conclusions. A brief discussion of the accuracy of centered differences for a monochromatic wave is given in appendix A, and details of the numerical choices made for diagnosing the effective diffusivity are given in appendix B.

2. The advection schemes

There are five advection schemes considered in this paper: the familiar second-order centered difference scheme, a pseudo-fourth-order scheme, first-order upwind, quicker, and FCT. Details of their numerical implementation are given in Pacanowski and Griffies (1999, henceforth *The MOM3 Manual*). This section provides a synopsis of their salient characteristics.

The second-order accurate centered-difference scheme (often abbreviated as simply ''centered differences'') conserves first and second moments. Under a steady-state, one-dimensional, advective-diffusive balance, if the Peclet number $\mathrm{Pe} = U\Delta/\kappa$ is larger than two, a computational mode will manifest, which tends to create unphysical extrema (Chen 1971; Bryan et al. 1975; Weaver and Sarachik 1990). In this expression, U is the maximum velocity scale, Δ is the grid spacing, and κ the tracer diffusivity. This constraint is one reason models with centered differences are run with nonzero tracer diffusion. However, the degree to which the scales of variability within the field being advected are resolved by the grid largely determines the extent to which this constraint is binding.

The upwind scheme is at the opposite end of the ''advection scheme spectrum'' from centered differences. It is monotonic, but it is highly diffusive and so does not conserve second and higher tracer moments. In one space dimension with a constant advection velocity and a leapfrog time step, the effective diffusivity is approximately $U\Delta/2$ (Molenkamp 1968; see also *The MOM3 Manual* for a review). For example, consider a 1° model at the equator with horizontal velocity $U = 20$ cm s^{-1}. The corresponding numerical horizontal diffusivity is roughly 10^8 cm^2 s^{-1}. As discussed in Griffies et al. (1998), such horizontal diffusion can create a tracer flux that dominates the flux parameterized with a vertical diffusivity A_v in regions where the isopycnal slope S is larger than $(A_v/A_h)^{1/2}$. With $A_v = 0.1$ cm^2 s^{-1} and $A_h = 10^8$ cm^2 s^{-1}, regions where $S \geq 3 \times 10^{-5}$, which is a common slope in the pycnocline, are regions where the horizontal upwind advection produces an effective diapycnal diffusion that swamps the physical pycnocline

diffusivity. If upwind advection is used in the vertical, with $U = 10^{-3}$ cm s^{-1}–10^{-2} cm s^{-1} and $\Delta = 1000$ cm, the vertical numerical diffusivity is roughly 0.5 cm^2 s^{-1}–5 cm^2 s^{-1}, which is again far too large for the pycnocline.

The pseudo-fourth-order advection scheme does a better job than the second-order scheme by reducing the amplitude of the unphysical dispersive extrema and reducing the phase errors of the flow features that are well resolved. The scheme implemented in MOM is based on the Geophysical Fluid Dynamics Laboratory (GFDL) SKYHI stratospheric GCM (compliments of J. Mahlman). It is not fully fourth order since the advecting velocity is second order while the quantity being advected is expanded to fourth order.

Quicker is third-order accurate in one space dimension. However, the implementation in MOM does not account for multiple dimensions, and so in practice it is only second-order accurate in space. It is based on the ''quick'' scheme of Leonard (1979), with some modifications whose details are provided by Holland et al. (1998). The MOM3 form of quicker is identical to that used in the ocean model component of the National Center for Atmospheric Research Climate System Model (Gent et al. 1998). Quicker does not conserve second moments and is not positive definite. Unphysical extrema are significantly reduced compared to the second-order centered difference scheme (e.g., Farrow and Stevens 1995; Holland et al. 1998).

The FCT scheme in MOM was implemented by C. Köberle and has been documented by Gerdes et al. (1991).[1] It is a combination of second-order centered differences and first-order upwind. The approach for obtaining the flux limiters is a slight modification of that described by Zalesak (1979). We refer the reader to these two papers for details. In general, since the flux limitations are applied only near extrema, the dispersive steepening, which can occur with centered differencing is still possible. Additionally, as discussed by Gerdes et al. (1991), the FCT scheme in MOM does not assure strict monotonicity of the advected quantity, and results may show unrealistic wavelike behavior depending on the settings of the flux limiters. Nonetheless, experience has shown that the solutions with FCT are quite smooth.

Although the precise computational timing for a model depends strongly on the details of the configuration, it is useful to provide an empirical estimate of the time required for the different advection schemes. Using just two tracers (temperature and salinity), various three-dimensional models run on the GFDL Cray T90 indicate the relative timings for the *full* model integration of 1, 1, 1.05, 1.10, 1.35 with the centered, upwind, fourth-order, quicker, and FCT schemes, respectively.

3. Numerical advection and convection

The purpose of this section is to articulate the basic issues associated with numerical advection and the preservation of water mass properties when coupled to convection.

The tool for illustrating these points is a one-dimensional advection-convection model, for which the advection velocity is assumed to oscillate periodically yet to be spatially constant. Without convection, centered advection schemes are reversible in the sense that if the oscillation has a frequency that is constant in time, then the dispersion errors accrued during one-half of the oscillation will cancel those accrued during the opposite half. However, as the dispersion errors are a function of the Courant number, if the oscillation frequency is time dependent, then the dispersion errors will not generally balance across a full cycle and they will instead accumulate over the course of many oscillation periods.

We are interested here in documenting how dispersion errors from numerical advection schemes couple to convection in a way to bring about an irreversible change in the water mass structure. There are numerous other sources of nonlinearities (e.g., advection by a spatially dependent velocity, feedbacks to the dynamics through pressure gradients, etc.). However, the presence of convection introduces very rapid and strong nonlinearities, which are always present in realistic ocean models, and which are traditionally ignored in idealized advection experiments.

The ease of examining advection schemes in one-dimension facilitates a great deal of intuition regarding their behavior under various scenarios. It is important to realize, however, that the results are at most suggestive; the extent to which the processes identified here are active in a particular three-dimensional ocean model requires careful examination.

The structure of the density profile in the model roughly corresponds to that which occurs in the equatorial thermocline (e.g., Pacanowski and Philander 1981), and the oscillation can be thought of as the seasonal cycle. The tracer and velocity placement on the vertical grid is identical to that employed in MOM.[2] The vertical grid spacing Δz is a uniform 33.3 m. The profile is advected through four grid spacings (133 m), with a vertically constant but temporally sinusoidal vertical velocity. A Courant number $U\Delta t/\Delta z = 0.7$ is used for the following experiments, where U is the maximum vertical velocity and Δt the model time step. While the exact parameters in this example are not physically realistic, they do serve to illustrate the interaction between dispersion and convection.

Numerous experiments have been run with this model using various advection schemes. After a single half-

[1] There is a typo in Eq. (A.2) of Gerdes et al. The centered advective flux portion of the scheme is actually computed with fields from time τ, rather than $\tau - 1$.

[2] Tracer and horizontal velocity points are on the same depth level, and vertical velocity is staggered. See *The MOM3 Manual* for details.

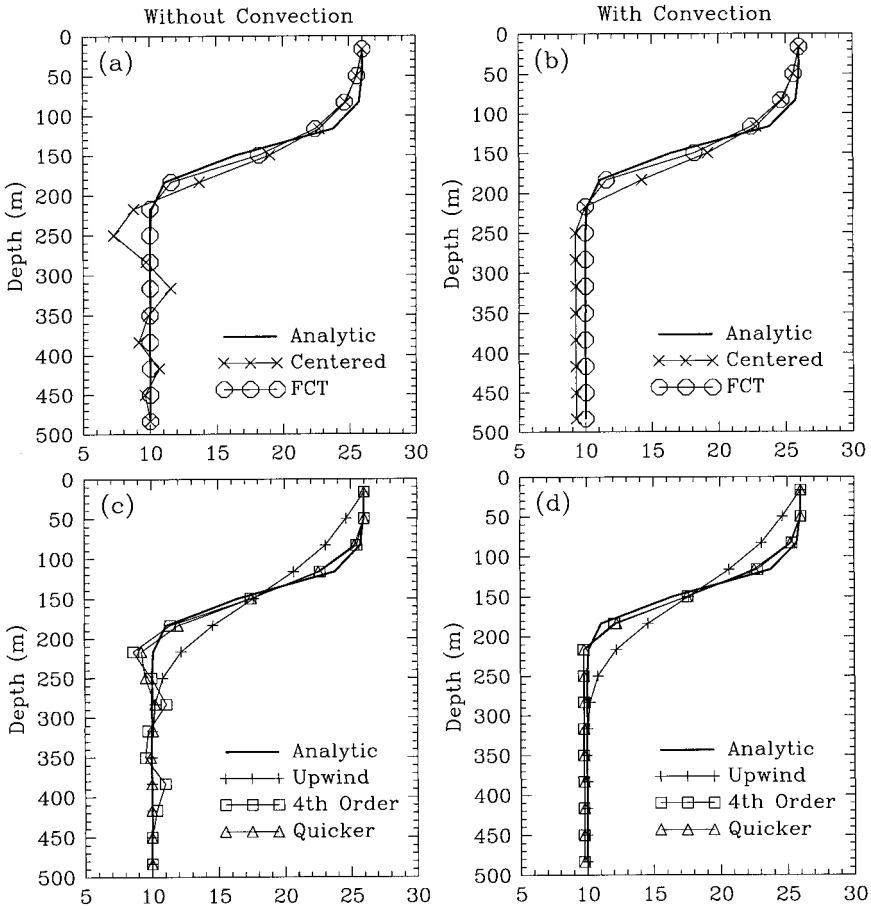

FIG. 1. Profiles of temperature after upward advection over one-half of the thermocline oscillation. The Courant number based on the maximum velocity is $U\Delta t/\Delta z = 0.7$, with a uniform vertical grid spacing $\Delta z = 33.3$ m. (a) FCT and centered advection alone without vertical convective adjustment. (b) FCT and centered advection with vertical convective adjustment. (c) Upwind, quicker, and fourth-order advection alone without vertical convective adjustment. Note that the fourth-order scheme is qualitatively similar to centered, yet the amplitude of the succession of dispersive extrema is reduced. The quicker scheme is characterized by fewer extrema than centered or fourth-order. (d) Upwind, quicker, and fourth-order advection with vertical convective adjustment. Notice that vertical convective adjustment acting on dispersive errors in the formally nondissipative centered scheme leads to a broadening of the thermocline and to an increase in the contrast between surface and deep temperatures. This effect is seen to a lesser degree for quicker and fourth order.

period of oscillation, the fundamentally dispersive nature of the centered advection scheme is readily apparent (Fig. 1a). The results from the fourth-order scheme and quicker are similar (Fig. 1c), yet with reduced amplitudes of the dispersive extrema. The FCT scheme has some dissipation (Fig. 1a), while the upwind scheme has significantly more (Fig. 1c).

The leading order truncation error with upwind differencing scales as (Δz), while the leading order errors with the other schemes scale as $(\Delta z)^2$ (see appendix A). Even though errors are smaller with a better resolved thermocline, they can be cumulative. In simulations of phenomena with intrinsic timescales of centuries, the aggregate effects of these errors can be significant for the leading order dynamics governing the global mean density structure. This is a general theme that recurs in this paper and it underlies the importance of minimizing spurious sources of mixing in ocean climate models.

Inclusion of convective adjustment in many ways eliminates the distinction between ''dispersive'' and ''dissipative'' schemes, as seen in Figs. 1b,d. A dispersive scheme effectively has significant nonlocal dissipation when the dispersive errors create gravitationally unstable profiles. Monotonic schemes are by definition unaffected by convective adjustment in the present demonstration (e.g., upwind in Fig. 1d). Based on this apparent equivalence, one might argue that FCT alone is roughly equivalent to centered differences combined

with convective adjustment. Both are based on the same second-order centered difference scheme, but each contains enough added dissipation, in the form of either upwind advection or convection, to eliminate unphysical density extrema. There is an important distinction, however, which breaks the equivalence. As seen in Fig. 1b, FCT effectively adds local diffusion, whereas convective adjustment acts on dispersively generated density maxima to nonlocally alter the weakly stratified abyss.

Convection induced by dispersively generated extrema acts to systematically cool the abyss relative to the surface. This process opposes the tendency for abyssal waters to be excessively warm due to, for example, aliasing of horizontal diffusion into diapycnal diffusion (Veronis 1977; Griffies et al. 1998), or to vastly excessive entrainment in overflows of dense waters from marginal seas (Winton et al. 1998). To the extent that this spurious cooling of the abyss from dispersive advection inducing convection is masking other model errors, numerical simulations may appear to be degraded in some ways by using a nondispersive advection scheme that eliminates the advection-convection errors.

The effect of convective mixing due to dispersion is both to broaden the thermocline in Fig. 1b, and to increase the contrast in density between the surface and the abyss. On large vertical scales, the second effect is dominant and buoyancy is effectively moved *upgradient.* This process can therefore be interpreted as negative mixing. The actual magnitude of the associated negative effective diffusivity is strongly dependent on the variability at the smallest scales, and the convective mixing acts to dissipate these scales even as it enhances the large-scale density contrasts. Note that the negative effective diffusivity does not indicate that the process is numerically unstable in the sense of a more traditional negative diffusivity process. We have more to say on negative effective diffusivities in section 4b.

Convective mixing is a nonlinear process. The vertical distance over which homogenization of the water column will occur is roughly $\Delta\rho|\partial\rho/\partial z|^{-1}$, where $\Delta\rho$ is the magnitude of the dispersively generated density extrema, and $\partial\rho/\partial z < 0$ is the stable vertical density gradient present before the spurious dispersive event. If second-order accurate vertical advection is the sole source of the density extrema, then the vertical extent of mixing scales as $(\Delta z)^2$. This scale arises from the truncation errors (e.g., see appendix A). The horizontal scaling should similarly go as $(\Delta x)^2$, assuming the regimes of flow do not change as the resolution is changed. The usual situation, however, is for an increase in horizontal resolution to be accompanied by a reduction in subgrid-scale friction. As such, the intensity of motion at the smallest scales will increase, and so the vertical extent of the spurious convective mixing may not be reduced at a higher horizontal resolution, unless the subgrid-scale parameters are held fixed.

4. Effective diapycnal mixing

The amount of spurious mixing in the previous one-dimensional example can be easily assessed through direct comparison with an analytical solution. Diagnosing such mixing for general three-dimensional flows requires a precise notion of effective diapycnal mixing and an associated effective diffusivity. For this purpose, we follow the work of Winters et al. (1995) and Winters and D'Asaro (1996).

Attention is limited to an incompressible fluid closed to boundary fluxes of mass or heat; momentum forcing is allowed. Additionally, the fluid is assumed to have a linear equation of state in order to focus on spurious mixing from advection, rather than introducing physical mixing sources from the nonlinear equation of state (McDougall 1987). Consequently, thermocline and pycnocline are synonymous in the following. Finally, the ocean bottom is assumed to be flat, although this assumption is not fundamental to the method.

a. The sorted fluid state

Available potential energy (APE) is the difference between a fluid's potential energy, $g \int d\mathbf{x}\, z\rho$, and the potential energy of a corresponding stably stratified reference state. The reference state is reached by adiabatically rearranging the fluid to a state of minimum potential energy, which is a state that contains zero horizontal density gradients. This rearrangement, or *sorting,* provides a mapping between the unsorted fluid density and the sorted fluid density: $\rho(\mathbf{x}, t) = \rho[z^*(\mathbf{x}, t), t]$. The sorting map determines a vertical position field $z^*(\mathbf{x}, t)$, which is the vertical height in the sorted fluid occupied by a parcel at $(\mathbf{x}, t)$ in the unsorted fluid (Winters et al. 1995; Winters and D'Asaro 1996). Due to the stable stratification in the sorted fluid, $z^*(\mathbf{x}, t)$ is a monotonic function of density $\rho(\mathbf{x}, t)$. Hence, there is a one-to-one relation between $z^*(\mathbf{x}, t)$ and $\rho(\mathbf{x}, t)$, which can be conveniently defined so that $\rho(\mathbf{x}_1, t) < \rho(\mathbf{x}_2, t)$ implies $z^*(\mathbf{x}_1, t) > z^*(\mathbf{x}_2, t)$. Here z^* is taken to be zero for the densest sorted parcel at the ocean bottom, and positive upward. In the following, it will be convenient to denote the density profile in the sorted reference fluid using the symbol $\rho_{\text{ref}}(z^*, t)$. As such, the sorting map between the unsorted and sorted fluids provides for the equivalence $\rho(\mathbf{x}, t) = \rho[z^*(\mathbf{x}, t), t] = \rho_{\text{ref}}(z = z^*, t)$.

b. The effective diapycnal diffusivity

In general, a tracer flux can arise from adiabatic and diabatic processes. Of interest here is the amount of flux $\mathbf{F}_D$ crossing a particular isopycnal surface. In particular, we consider the averaged diapycnal flux

$$F^{\rho} = \frac{1}{A} \int_{\rho} dS\, \hat{\boldsymbol{\rho}} \cdot \mathbf{F}_D, \tag{1}$$

where dS is the differential area element for an isopycnal surface, $\hat{\boldsymbol{\rho}} = \nabla\rho/|\nabla\rho|$ is a unit vector pointing in the diapycnal direction, and A is the horizontal cross-sectional area of the fluid domain. As seen in the following, F^ρ provides a useful measure of the rate (F^ρ has units of *velocity* $\times$ *density*) of water mass mixing occurring across a particular isopycnal surface. It is important to note that the total area of an isopycnal surface, $A_\rho = \int_\rho dS$, is generally different than the horizontal area A of the fluid domain, unless all isopycnals are completely flat. In particular, light density surfaces that exist only in a portion of the domain will typically have smaller areas than A, and heavy surfaces will have larger areas. As such, for a constant flux $\hat{\boldsymbol{\rho}} \cdot \mathbf{F}_D$ passing across a density surface, F^ρ will be smaller or larger than this flux depending on whether A_ρ is smaller or larger than A. In general, the area A_ρ is nontrivial to compute, especially in a level or sigma model, due to corrugations or undulations in the density field. In contrast, as shown below, the flux F^ρ is easily computed using standard algorithms. This detail concerning the area normalization makes the present scheme ideal for our purposes.

1) Effective diapycnal mixing associated with diffusion

To help interpret the effective diapycnal mixing from numerical representations of advection, we will find it useful to compare such results with those arising from horizontal and/or vertical diffusion. For this purpose, consider the averaged diapycnal flux F^ρ resulting from a flux $\mathbf{F}_D = -(A_h\nabla_h\rho + \hat{\mathbf{z}}A_v\partial_z\rho)$, where A_h and A_v are nonnegative horizontal and vertical diffusivities, respectively. Assume that the unsorted density surfaces are stably stratified, which is the case for all initial conditions considered in the subsequent model experiments. Hence, the area element takes the form $dS = dx\,dy\,\sqrt{1+\sigma^2}$, where $\sigma = |\nabla_h\rho|/|\rho_z|$ is the magnitude of the isopycnal slope, and $1 + \sigma^2 = |\nabla\rho|^2(\partial_z\rho)^{-2}$. With $\hat{\boldsymbol{\rho}} \cdot \mathbf{F}_D = -[A_h|\nabla_h\rho|^2 + A_v(\partial_z\rho)^2]|\nabla\rho|^{-1} = (A_h\sigma^2 + A_v)|\rho_z|(1+\sigma^2)^{-1/2}$, the diapycnal flux can be written

$$\begin{aligned} F^\rho &= -\frac{1}{A}\int_\rho dx\,dy\,(\sigma^2 A_h + A_v)|\rho_z| \\ &= -\left[\frac{1}{A}\int_\rho dx\,dy\,(\sigma^2 A_h + A_v)(N/N_*)^2\right]\frac{\partial\rho_{\text{ref}}}{\partial z^*} \\ &\equiv -\kappa_{\text{eff}}(\rho, t)\frac{\partial\rho_{\text{ref}}}{\partial z^*}. \end{aligned} \tag{2}$$

In this expression, N and N_* are the buoyancy frequencies for the stably stratified unsorted and sorted fluid, respectively, and the integral is over the horizontal projection of the isopycnal surface ρ = constant. Introduced here is a nonnegative effective diapycnal diffusivity $\kappa_{\text{eff}}(\rho, t)$. This diffusivity weights the vertical gradient of the stably stratified sorted fluid $\partial\rho_{\text{ref}}/\partial z^* = -\rho_o N_*^2/g < 0$. As such, the diapycnal flux F^ρ corresponding to pure horizontal and vertical diffusion is a positive flux (toward larger z^*) of sorted density $\rho_{\text{ref}}(z^*, t)$ at a sorted vertical position z^*.

For the case with vertical diffusion alone, if the average of the squared buoyancy frequency for the unsorted fluid is larger than the squared buoyancy frequency for the sorted fluid, then $\kappa_{\text{eff}} > A_v$; that is,

$$\text{If } N_*^2 \le A^{-1}\int_\rho dx\,dy\,N^2 \quad \text{then } A_v \le \kappa_{\text{eff}}. \tag{3}$$

This inequality can be satisfied, for example, when a density surface extends from regions of strong vertical stratification (as in the low latitudes) into regions of very weak stratification (as in the high latitudes). Model experiments given in sections 5 and 6 provide relevant illustrations of this point.

Another way to increase the effective diffusivity was discussed by Winters and D'Asaro (1996) for the case of isotropic diffusion. In their examples, the slope term appearing in Eq. (2) becomes important in regions where density surfaces are highly corrugated or stretched, such as occurs for steep waves (see Winters and D'Asaro for the case of vertically overturning waves). Conversely, as mentioned earlier, the effective diffusivity can be small simply because the surface area of the particular density surface is small. Finally, as expected, the effective diapycnal diffusivity corresponding to horizontal diffusion increases as the isopycnal slopes steepen.

2) Effective mixing in the general case

For a numerical experiment using a perfect advection scheme, with no other tracer transport and with zero buoyancy fluxes at the boundaries, a fluid parcel will preserve its density: $\partial_t\rho + \mathbf{u}\cdot\nabla\rho = 0$. In turn, the sorted density ρ_{ref} is static: $\partial_t\rho_{\text{ref}} = 0$, and it follows that there is a zero diapycnal flux F^ρ. Conversely, any temporal change in the sorted reference density reflects changes in the water mass census. These changes are the direct result of diapycnal mixing associated with nonzero convergence of F^ρ, and κ_{eff} is the nonzero diffusivity setting the strength of F^ρ. These considerations lead to the evolution equation for the sorted density

$$\frac{\partial\rho_{\text{ref}}}{\partial t} = \frac{\partial}{\partial z^*}\left(\kappa_{\text{eff}}\frac{\partial\rho_{\text{ref}}}{\partial z^*}\right). \tag{4}$$

This is the basic equation that will be used to quantify the mixing of density in the following.

In summary, the effective diffusivity κ_{eff} is computed as follows. First, the density is sorted using an algorithm such as that found in Press et al. (1992). Keeping track of the volume of the fluid parcels when sorting allows for the z^* field to be computed as well, using the horizontal cross-sectional area A of the fluid domain to convert volume to height. Next, $\kappa_{\text{eff}}(z^*, t)$ is diagnosed

from the time tendency of ρ_{ref} and its vertical gradient according to the diffusion equation (4). It is noted that an integral over an isopycnal surface in the unsorted fluid is equivalent to a horizontal integral in the sorted fluid, since surfaces of constant ρ are equivalent to surfaces of constant z^*. As such, the effective diffusivity κ_{eff} is equivalently a function of (ρ, t) or (z^*, t), and so κ_{eff} provides a direct measure of the effective diapycnal diffusivity as a function of density. Note that in general it is not necessary to assume anything regarding the slope of the isopycnals, since the sorted density profile is defined for any arrangement of the unsorted isopycnal surfaces. Further numerical details concerning this calculation are given in appendix B.

3) SOME FURTHER COMMENTS

The effective diffusivity diagnostic provides a quantitative estimate of the modification of the fluid's density distribution. By rearranging or sorting density into classes, the evolution of the resulting one-dimensional sorted density profile is modeled with a second-order diffusion operator, which acts in the space of the sorted density. This approach allows for an association between a nonzero effective diffusivity and density transport occurring between these classes.

Since the effective diffusivity is diagnosed local to the region between any two particular density classes, its value varies in the sorted density space as well as time. Mixing between two classes contributes to an increase in potential energy of the sorted fluid, and hence is associated with a local positive effective diffusivity. This is the case where diffusion is the transport mechanism. In contrast, the spontaneous creation of an extreme density class or the increase of gradients between the classes is associated with a negative effective diffusivity, local to the region in sorted density space where the new extrema or increased gradient occurs. Notably, a locally negative effective diffusivity does not necessarily signal the presence of an exponentially growing mode, which would be the case if a negative diffusivity were active globally throughout the sorted density space.

Dispersive advection schemes have odd order leading truncation errors [e.g., Eq. (A1) in appendix A for second-order centered differences], and so are not appropriately modeled by a second-order diffusion operator. Nevertheless, the key point is that by being able to either introduce extreme density classes or increase gradients in the density distribution, dispersive advection schemes will always admit regions of locally negative effective diffusivities. If the advection scheme is conservative, the amount of artificially positive anomalous density created will locally match the amount of negative anomalous density created. In this manner, the dispersion is analogous to a conservative negative mixing process. Hence, a locally negative effective diffusivity is a sensible means of summarizing this spurious process.

c. *Z-model experiments*

The previous formalism is applied to various *z*-model experiments in sections 5 and 6. The goal is to quantify the levels of spurious mixing associated with transport occurring in various flow states. Although our focus is on advection schemes, it should be understood that coupling to convection and other nonlinearities can, and will, cause further irreversible modifications to water masses.

The experiments focus on the pycnocline region for three reasons. First, it is here that measurements from Ledwell et al. (1993) provide evidence for small diapycnal rates of mixing in certain ocean regions. Second, the presence or absence of spurious mixing in the deeper ocean is arguably of less relevance to climate model simulations than that occurring in the pycnocline region, simply because the deeper ocean is typically much less stratified. Third, there is growing evidence of enhanced mixing above rough topography (Polzin et al. 1997), in marginal basins strongly influenced by tides (Ledwell et al. 1991), and near seamounts (Toole et al. 1997), thus motivating us to focus on advection in the largely ideal ocean interior. For these reasons, the experiments in sections 5 and 6 employ a flat bottom with straight lateral boundaries, thus eliminating potential issues involving irregular bottom and side boundaries. Issues of model-represented bottom topography are mentioned in section 7.

In general, the experimental design is the following. First, the model is integrated for some time to place it into a particularly interesting flow regime. Next, the model is run just for a few time steps without buoyancy forcing and without convective adjustment. During this time, the effective diffusivity formalism is used to quantify the levels of effective diapycnal mixing associated with various model transport processes such as advection, vertical diffusion, and horizontal diffusion. As discussed previously, the effective diapycnal mixing associated with vertical diffusion depends on the stratification. Hence, to provide a benchmark for judging the effective diapycnal mixing arising from advection and horizontal diffusion, we compare their results to those from vertical diffusion. For the coarse resolution sector model in section 5, we use $A_v = 0.1$ cm^2 s^{-1} as a nominal background, and for the fine resolution eddy permitting channel in section 6, we use $A_v = 0.2$ cm^2 s^{-1}. Both of these numbers are roughly consistent with the measurements of Ledwell et al. (1993).

Upon turning off buoyancy forcing, the model will undergo an adjustment process, whose details depend on the model configuration and initial flow regime. Such transients, which can be sizeable, are arguably relevant for realistic climate variability and climate change experiments. Although the effective diffusivities diagnosed from these experiments are not exactly those that may be present in the fully forced experiments, the re-

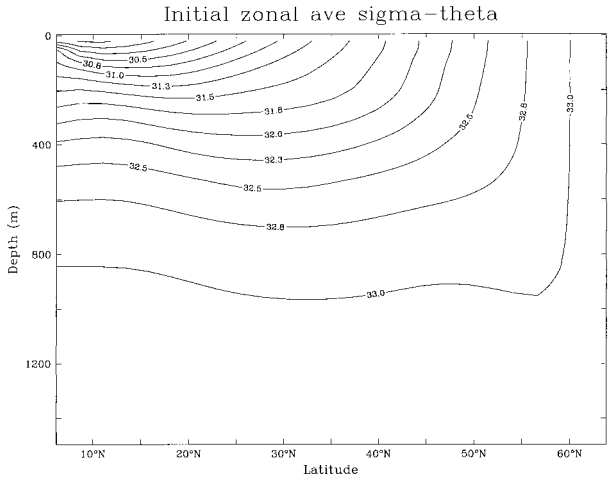

FIG. 2. A zonal average of the σ_θ field used for the standard sector model experiments. The horizontal resolution is a uniform 2.4° in the longitude and latitude, and the domain is 60° × 60°. Only the upper 1500 m of the 4000-m-deep model is shown (this represents 14 of the 18 vertical levels); the deeper regions are very weakly stratified. Density is given by $\rho = \rho_o(1 - \alpha\theta)$, where $\rho_o = 1.035$ g cm^{-3}, $\alpha\rho_o = 2.55 \times 10^{-4}$ g cm^{-3} °C^{-1}, and $\sigma_\theta = 1000(\rho - 1)$. This particular model solution was obtained by running for 5000 yr with a horizontal diffusivity of $A_h = 10^7$ cm^2 s^{-1}, vertical diffusivity of $A_v = 0.5$ cm^2 s^{-1}, horizontal viscosity of 5×10^8 cm^2 s^{-1}, zero bottom drag, vertical viscosity of 10 cm^2 s^{-1}, advection using centered differences, zonal wind forcing as given by F. Bryan (1987), and restoring to the linear surface density profile of Cox and Bryan (1984). The restoring time is 50 days over the upper 30-m thick box, which corresponds to roughly 28 W m^2 °C^{-1}. A 1-day time step is used for the tracers, and a 1-h time step for both the barotropic and baroclinic modes. The barotropic mode was solved using the rigid-lid streamfunction method (Bryan 1969). The model grid is identical to that employed by Griffies et al. (1998) and Griffies (1998).

sults should nonetheless provide a fair indication of what can occur under certain regimes with forcing.

5. Spurious mixing in a coarse sector

The first example is a coarse resolution sector model spun up with constant zonal winds using thermal restoring at the surface.

a. Standard model configuration

The standard version of this model consists of the same grid used in the Griffies et al. (1998) and Griffies (1998) papers. Note that the vertical grid is stretched using a cosine function. As shown by Treguier et al. (1996), such analytic stretching ensures that the truncation errors, at least for the second-order centered scheme, maintain the same behavior as when using a uniform vertical grid.

Further details of the model configuration are given in the caption to Fig. 2. This figure shows a zonal mean from the model solution used as the initial condition for the experiments to be run without buoyancy forcing. In the horizontal, the solution consists of a two-gyre circulation with a western boundary current (Fig. 3) and deep water formation in the far north (Fig. 2). Figure 4 shows the corresponding sorted density profile obtained by sorting the three-dimensional density field in Fig. 2, and then averaging to the same discrete vertical levels used in the unsorted model (see appendix B for more details).

1) EFFECTIVE DIAPYCNAL DIFFUSIVITY

Figure 5 shows the time-averaged effective diapycnal diffusivity obtained by running the model for 20 time steps without buoyancy forcing and without convective adjustment. The results for each time step differ only slightly over these 20 steps.

For the case of vertical diffusion alone, note the small values of κ_{eff} near the surface. The reason for these small values is due to the small surface area occupied by the low density water, and the normalization in Eq. (1) by the area of the model domain, rather than the area of an isopycnal surface. Likewise, κ_{eff} at depth reaches above 0.1 cm^2 s^{-1}, reflecting the satisfaction of the inequality (3) for these isopycnals. Nearly identical results are obtained in experiments run with isotropic diffusion (not shown), where $A_v = A_h$. The only exception is for very weakly stratified regions, in which the isotropic case shows slightly larger κ_{eff} because of added horizontal mixing across steeply sloped isopycnal layers.

The case of horizontal diffusion alone, with $A_h = 10^7$ cm^2 s^{-1}, shows a steady increase in κ_{eff} with depth, as a result of the relatively large areas with steep isopycnal slopes within the denser layers. Even in the upper thermocline region, the effective diffusivity reaches well above that seen with $A_v = 0.1$ cm^2 s^{-1}. These large values for the diapycnal mixing point to the well-known problems with horizontal background diffusion, sometimes added to models in order to stabilize an unstable isoneutral diffusion scheme (see Griffies et al. 1998), or to reduce dispersion errors associated with some advection schemes. Such mixing can lead to the Veronis effect (Veronis 1975, 1977), which is an unphysical dynamic balance between vertical advection and horizontal diffusion aliased as diapycnal diffusion. The Veronis effect generally occurs in models as a result of too much mixing across isopycnals next to western boundaries.

The spurious mixing diagnosed for the second-order, fourth-order, and quicker advection schemes are largely identical, with the fourth-order scheme showing somewhat smaller $|\kappa_{\text{eff}}|$. What is most distinctive is their large negative effective diffusivities in the lower thermocline. As discussed in section 4, $\kappa_{\text{eff}} < 0$ corresponds to the local creation of new extreme density classes or the strengthening of gradients between these classes, both of which can occur through advection dispersion errors. In the upper thermocline (above 500 m), note the rather small values for each of these three schemes, where $|\kappa_{\text{eff}}|$ is smaller than that realized from the $A_v = 0.1$ cm^2 s^{-1} experiment.

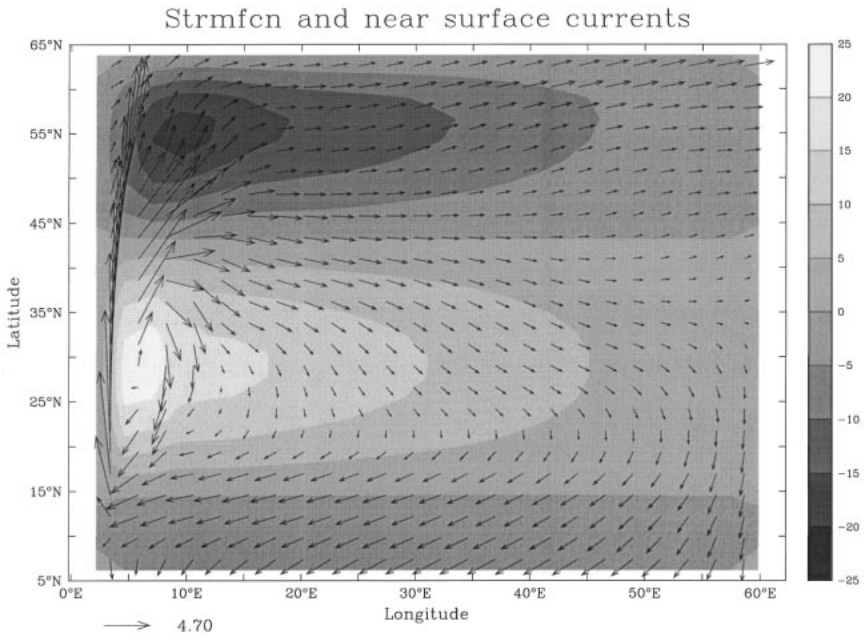

FIG. 3. Barotropic streamfunction in units of Sv (10^6 m^3 s^{-1}) for the standard sector experiment at the end of its 5000-yr spinup. Also shown are the level 2 velocities (depth = 53 m; beneath the surface Ekman layer), where every velocity point is shown. The Rossby number (using the gyre-scale to define a length and velocity scale) is quite small throughout the flow. Importantly, note the presence of only a single velocity point in the western boundary region. The scaling magnitude (cm s^{-1}) of a vector is shown at the bottom left.

The upwind scheme exhibits an effective diffusivity which is similar in structure and magnitude to horizontal Laplacian diffusion. This behavior is expected since the upwind scheme's leading order truncation terms are diffusive (Molenkamp 1968). FCT shows positive effective diffusivities for all levels, and it is quite similar to the upwind scheme in the upper 500 m of the sorted water column. It has notably smaller diffusivities in the lower thermocline, however. Comparison of the FCT results with various pure vertical diffusion experiments indicate that FCT, for the thermocline region of this particular experiment, can be associated with a vertical diffusivity in the range $A_v = 0.3$ cm^2 s^{-1} to 0.4 cm^2 s^{-1}.

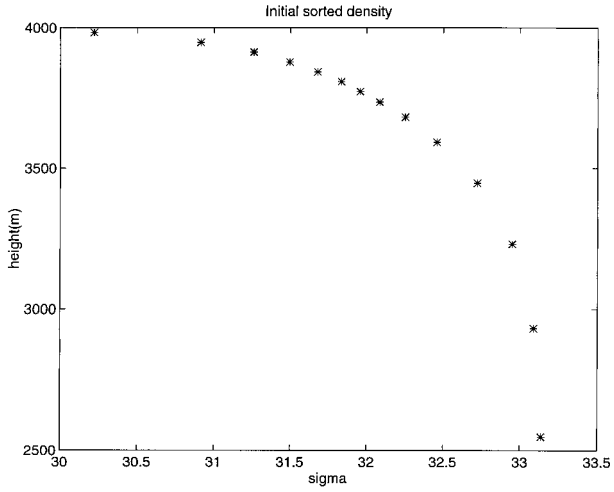

FIG. 4. The initial sorted sigma profile for the standard sector model (Fig. 2). Shown here is the upper 1500 m only (14 of the 18 levels). The stratification for the lower 2500 m is quite weak. The ''upper thermocline'' is roughly that portion of the profile within 500 m of the surface. The vertical axis is measured from the ocean bottom, whereas that in Fig. 2 is from the surface.

2) WESTERN BOUNDARY

The effective diffusivity diagnostic provides a measure of the spurious mixing across a particular isopycnal. To diagnose the mixing occurring along regions of a particular isopycnal, we rely on visual inspection of the three-dimensional density field. This inspection indicates that numerical problems are localized in the western boundary region. This result might be expected, since it is at the western boundary where the strongest horizontal currents and strongest shears are present. To illustrate this point, Fig. 6 shows a zonal-vertical section at 20°N and next to the western boundary. 20°N is in the southern portion of the model's subtropical gyre (Fig. 3). In this region, the horizontal currents exhibit a strong anticyclonic motion with intense upwelling next to the wall, downwelling in the interior, and zonal currents directed toward the wall. The solution shown is that realized after 200 time steps, starting from the same smooth initial condition shown in Fig. 2. Recall that the initial condition is obtained from a solution using hor-

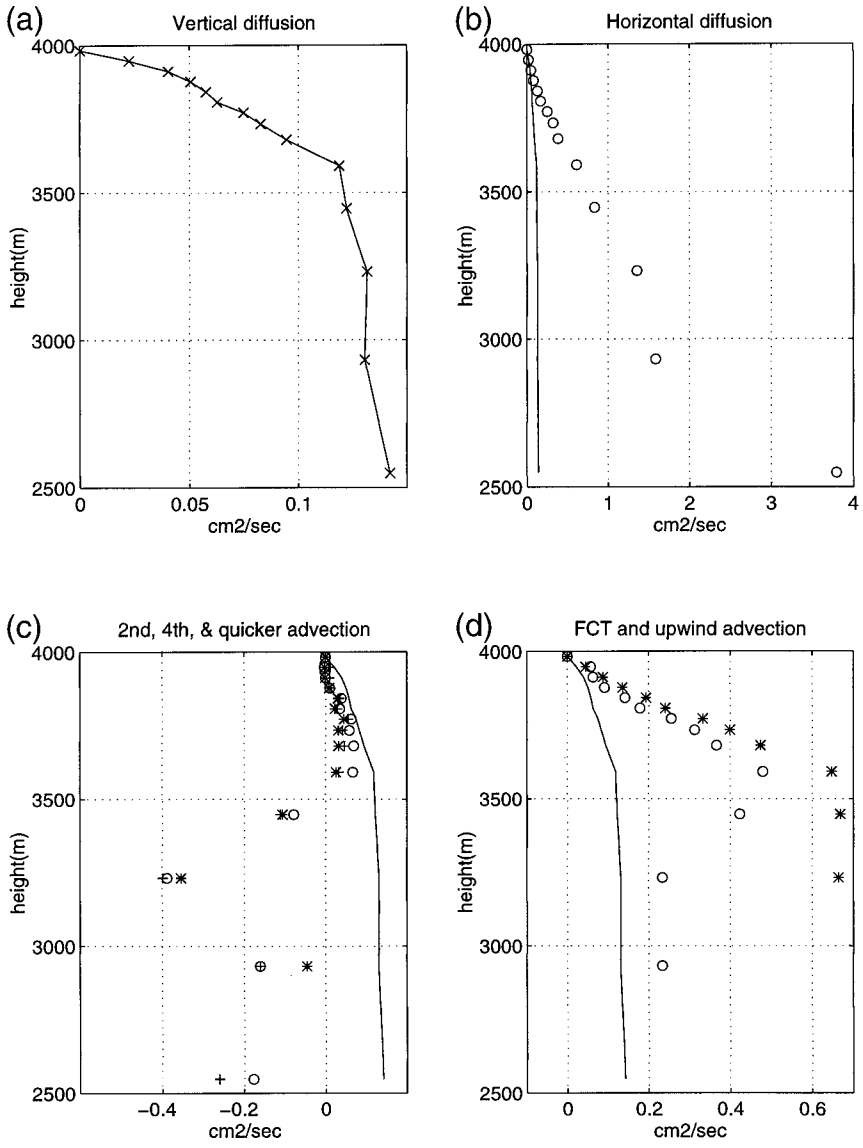

FIG. 5. Effective diapycnal diffusivities κ_{eff} ($\text{cm}^2\ \text{s}^{-1}$ abscissa) for the standard sector model as a function of distance from ocean bottom (ordinate). Note the different horizontal scales, and the presentation of only the top 1500 m (14 of the 18 levels) of the model. Convective adjustment and buoyancy forcing have been removed, yet the same wind used in the spinup is maintained. Each $\kappa_{\text{eff}}(z^*)$ profile is obtained by taking the time mean from each day of a 20 day experiment. The values for κ_{eff} at each of the 20 days do not differ substantially from those shown here. (a) Vertical diffusion alone with $A_v = 0.1\ \text{cm}^2\ \text{s}^{-1}$. This result is superimposed on all the other panels to set a benchmark of what constitutes an acceptably small value for the effective diffusivities. (b) Horizontal diffusion alone (○) with $A_h = 10^7\ \text{cm}^2\ \text{s}^{-1}$. (c) Advection alone, with the centered (○), fourth-order (*), and quicker (+) schemes. (d) Advection alone with FCT (○) and upwind (*).

izontal diffusion. Hence, the strong amount of vertical motion next to the western wall (on the order of 5–10 km day^{-1}) is largely asociated with the Veronis effect.

Although the second-order, fourth-order, and quicker schemes show a very small amount of effective mixing in the upper 500 m (Fig. 5), Fig. 6 indicates that the solutions with these schemes soon loose their three-dimensional integrity. The schemes are unable to maintain the stong gradients associated with this boundary current, and the problems extend out roughly 10°–12° from the western wall (four to five grid points). The FCT scheme, on the other hand, acts to suppress this signal in a manner similar to the horizontal diffusion used in the original spinup. Hence, its solution remains relatively smooth.

In conclusion, for this particular grid and flow regime,

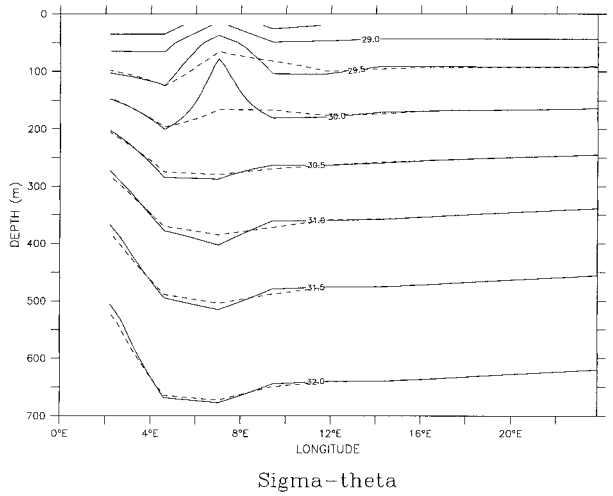

FIG. 6. Zonal-vertical slice at 20°N for the standard sector model ($\Delta\lambda = \Delta\phi = 2.4°$, 18 vertical levels). Shown here is the σ_θ field after 200 days of integration. The solution with the large amplitude signal (solid line) is that from second-order centered advection; the smoother solution (dashed line) is from FCT. The solution obtained from the fourth-order scheme (not shown) is very similar to the second-order scheme, with a slightly smaller amplitude. The quicker solution (not shown) is again similar to the second- and fourth-order schemes, with still smaller, yet nontrivial, signal. The upwind solution (not shown) is very similar to the FCT result.

the given advection schemes are unable to satisfy the competing constraints of keeping the effective mixing equivalent to that realized with $A_v \approx 0.1$ cm^2 s^{-1} while maintaining minimal dispersion errors. Additionally, as seen by Fig. 6, the isopycnally averaged effective diffusivity for FCT arises mostly from mixing in the region near the western boundary current, and it extends eastward over a 10°–12° region. As such, an effective mixing coefficient local to the western wall is much greater than the averaged values reported in Fig. 5. A rough estimate suggests that local values reach up to 2 cm^2 s^{-1}. This conclusion is potentially significant due to the dynamical implications pointed out by Veronis (1975, 1977) associated with diapycnal diffusion next to western boundaries. Furthermore, if one contends that there is enhanced diapycnal mixing next to boundaries in the real ocean, then a rational approach to studying this mixing in models is through the direct use of an enhanced vertical diffusivity, as employed by Marotzke (1997), rather than from the spurious, and possibly pathological, numerical sources described here.

b. Increased resolution

To illustrate how added grid resolution affects the amount of spurious mixing in the sector model, we now consider two experiments with the identical subgrid-scale parameters but with increased grid resolution. Each of the new experiments was individually spunup for 5000 yr and then the effective mixing diagnosed as before.

1) VERTICAL RESOLUTION

As previously described, the main source of spurious mixing from the FCT scheme is associated with the western boundary region. As such, an increase in vertical resolution should not significantly alter the results shown in Figs. 5 and 6. Indeed, doubling the vertical resolution (36 vertical levels, where each vertical Δz is halved relative to the standard model) gives results (not shown), which are quite similar to those in the standard 18-level experiment. The main improvement with increased vertical resolution is a reduction in the magnitude of the negative κ_{eff} at depth for the second, fourth, and quicker schemes.

2) HORIZONTAL RESOLUTION

Keeping the vertical resolution fixed, doubling the horizontal resolution ($2.4° \rightarrow 1.2°$), and holding all the subgrid-scale parameters unchanged allows for a better resolution of the western boundary current structure. Figure 7 shows the barotropic streamfunction and near-surface currents for this higher horizontal resolution case. Note in particular the presence of at least two velocity points within the western boundary region, as compared to one point in the 2.4° model shown in Fig. 3. Figure 8 shows that the problematical western boundary region is not severely distorted by the centered advection scheme alone, in contrast to the solution in Fig. 6 obtained with 2.4° resolution. Correspondingly, the effective diffusivity for each advection scheme is significantly smaller (Fig. 9). Note especially the significant improvements for the FCT and fourth-order schemes. The slight negative values for κ_{eff} at depth for the FCT scheme can be attributed to a small amount of dispersion associated with its centered component and the larger vertical grid boxes at depth. This result illustrates an important point: there are many ''flavors'' to FCT, which may show slightly different results. The extent to which the flux limiters are set largely determines the amount of upwind employed by the scheme. Analysis of the three-dimensional solution (not shown) indicates that the FCT solution is well behaved, at least after the 200 days of this experiment. The slightly negative κ_{eff}, therefore, appears to be of minor consequence here.

c. Resolution of the western boundary currents

Along the western wall, there is a frictional boundary layer whose width is given by (Munk 1950)

$$L_M = \frac{\pi}{\sqrt{3}}(A_m/\beta)^{1/3}, \tag{5}$$

where A_m is the horizontal viscosity and β is the planetary vorticity gradient. As noted by Bryan et al. (1975), not resolving this *Munk boundary layer* can result in a computational mode that generates a checkerboard pat-

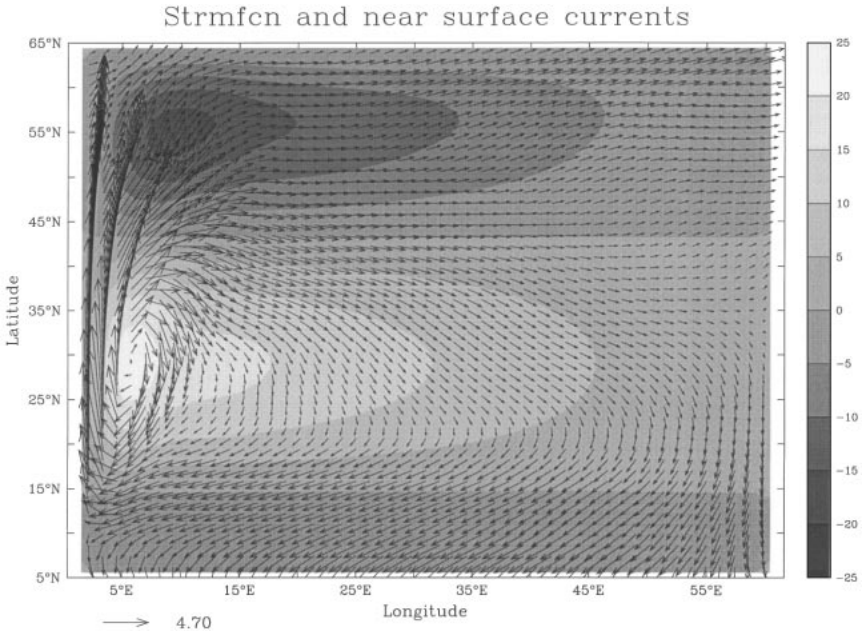

FIG. 7. Barotropic streamfunction in units of Sv for the 1.2° sector experiment at the end of its 5000-yr spinup. Also shown are the level 2 velocities (depth = 53 m; beneath the surface Ekman layer), where every velocity point is shown. Note the presence of at least two velocity points in the western boundary region. The scaling magnitude (cm s^{-1}) of a vector is shown at the bottom left.

tern in the rigid lid's barotropic streamfunction. As seen in the following, this width provides a relevant scale for which to judge the resolution of the western boundary current.

The standard 2.4° sector model used a horizontal viscosity of $A_m = 5 \times 10^8$ cm^2 s^{-1}. The minimum width of the Munk boundary layer (occurring in the southern part of the gyre) is roughly 240 km, which is close to the grid resolution. The result, as seen in Fig. 3, is a subtropical gyre consisting of a strong, narrow meridional jet next to the wall, with a strong southward flow just two grid points away. The tracer field and barotropic streamfunction are quite smooth with this configuration when using a horizontal tracer diffusivity of 10^7 cm^2 s^{-1} and any of the five advection schemes. Additionally, if FCT advection is used, the horizontal diffusion can be turned to zero without visibly compromising the integrity of the solution. Nonetheless, the results in Fig. 5 indicate that the solution also contains a nontrivial amount of spurious mixing: the effects of horizontal diffusion at the western wall are largely replaced by the upwind component of FCT. In contrast, the 1.2° model resolves the western boundary current with roughly two grid points (Fig. 7). Figure 9 suggests that such resolution is adequate for maintaining a small amount of spurious mixing associated with advection due to the reduction of dispersion errors. Experiments (not shown) have indicated that another way to ensure that the spurious advective mixing is small is to increase the horizontal viscosity while maintaining the same grid resolution. The relation (5) shows that the Munk boundary layer will be broadened, thus allowing the grid to better resolve the western boundary current.

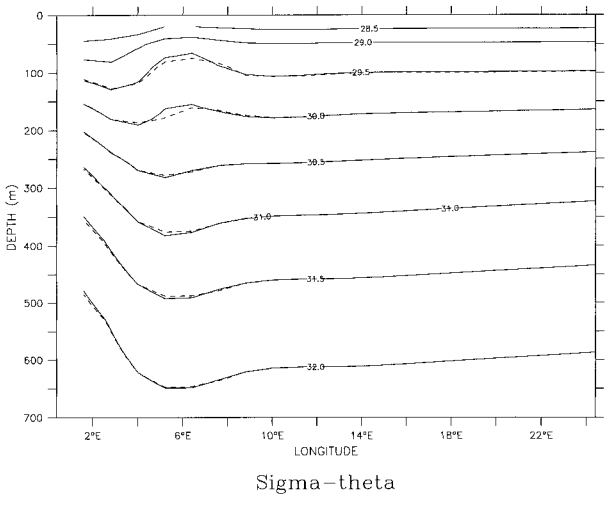

FIG. 8. Zonal-vertical slice at 20°N for the 1.2° sector model with 18 vertical levels. Shown here is the σ_θ field after 200 days of integration with second-order (solid) and FCT (dashed) advection. Compare this result with that in Fig. 6 from the standard 2.4° experiment.

The central conclusion from these coarse-resolution experiments is the following: although the model stability and visual integrity (i.e., smoothness) may be maintained with a relatively small viscosity and a dis-

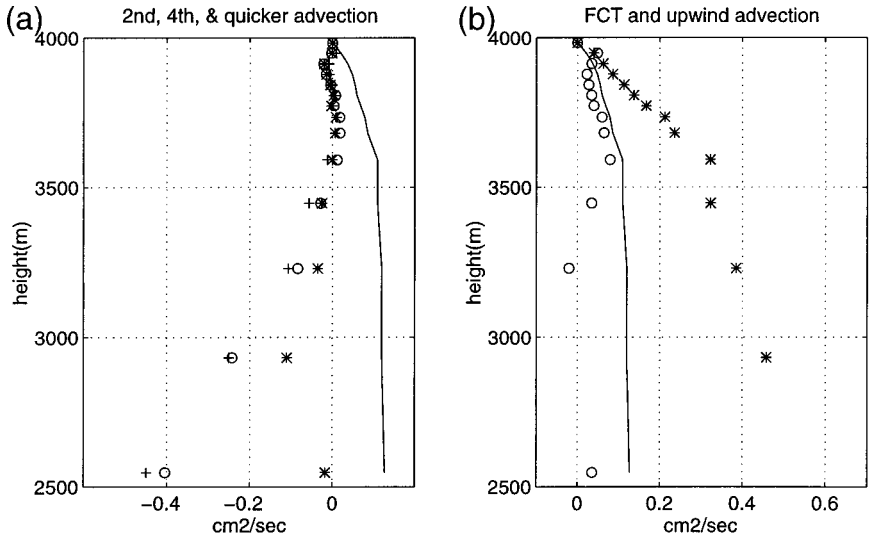

FIG. 9. Effective diapycnal diffusivities κ_{eff} (cm^2 s^{-1}, abscissa) for the 1.2° sector model with 18 vertical levels. (a) Advection alone with centered (○), fourth-order (*), and quicker (+). (b) Advection alone with FCT (○) and upwind (*). Each of the plots also shows the result for the vertical diffusion alone with $A_v = 0.1$ cm^2 s^{-1} (solid line). Note that the results for the vertical and horizontal diffusion experiments are almost identical to those in the 2.4° model (see Fig. 5).

sipative advection scheme such as FCT, the resulting scales of motion may not be resolved sufficiently. In this situation, the dissipative advection scheme will be forced to employ an unphysically large amount of spurious mixing. For the experiments considered here, a resolution of roughly two grid points in the Munk layer reduces this mixing to a negligible level.[3]

6. Spurious mixing in an eddying channel

There are an increasingly large number of primitive equation *z*-model studies that admit some representation of quasigeostrophic eddies. Due to the relatively strong velocity shears and tracer gradients in such flows, the integrity of the solution is largely dependent on the quality of the numerics. Farrow and Stevens (1995), for example, provide a vivid example of problems that may occur under eddying flow regimes when using second-order centered advection without enough explicit dissipation.

In the presence of quasigeostrophic eddies, there will be a transfer of tracer variance and enstrophy toward the grid scale (for reviews see, e.g., Rhines 1977; Salmon 1998). In contrast, for coarse simulations without eddies, so long as the friction is held fixed, no new scales of motion are introduced as the grid resolution is increased. Hence, it is possible to eventually resolve all flow structures in the absence of eddies, but not so with eddies. This is a fundamental difference between the coarse experiments considered in section 5 and those considered in this section.

Two central goals of eddy-permitting ocean modeling are to realize a nontrivial resolved cascade of enstrophy and variance throughout the scales larger than the grid scale, and to adequately dissipate the cascade as it reaches the grid scale. The alternative is to either overdissipate, and hence overdamp the eddies that are of physical interest, or to underdissipate, which can reduce the solution to a ''sea of numerical grid noise.''

To address the above dual goals, modelers have tended to take two approaches. Traditionally, the use of higher-order operators, such as the biharmonic operator (e.g., Semtner and Mintz 1977), have been found to be useful. The reason is that these operators are more scale selective than the Laplacian operator; that is, they weakly damp the large scales and strongly damp the small scales. An alternative approach, thoroughly articulated by Shchepetkin and McWilliams (1998), is to build the dissipation of enstrophy and variance directly into the numerical advection operator, thus making an extra dissipation operator unnecessary. This approach is relatively new to ocean modeling, yet it holds the promise of providing even more scale-selective algorithms than achieved with higher-order operators.

The two stated goals capture the central numerical issues involved with simulations of two-dimensional turbulence or quasigeostrophic turbulence using isopycnal layered models. Consequently, transport schemes for geophysical fluid modeling have been typically designed just with these two goals in mind. However, for three-dimensional models not based on the isopycnal layer framework, it is essential that the third goal of allowing only a small amount of

[3] This result may be dependent on MOM's B-grid, and so other grids may require less or more grid points.

spurious diapycnal mixing also be considered. Achieving an advection-dissipation scheme that satisfies the first and second goal does not imply that it satisfies the third goal. This is the key point to be taken from the following analysis.

The purpose of this section is to illustrate the above points in the context of a flat bottom thermally forced channel model. For this purpose, numerous experiments are run in which we change the horizontal and vertical resolution, horizontal viscosity and diffusivity, and advection scheme.

a. The channel model

The channel model extends from 10°S to 40°S, it is 10° in longitude, and 1200 m deep. The horizontal resolution is locally square, so that the latitudinal resolution $\Delta\phi$ is given by $\cos\phi\ \Delta\lambda$, where $\Delta\lambda$ is the constant longitudinal resolution. The vertical resolution is uniform from the surface to the bottom. The model is forced at the surface with the same Cox and Bryan (1984) temperature profile used for the sector model, yet with the weaker restoring of 23 W m^{-2} °C^{-1}. There is no wind stress and no bottom stress. Each case used the same vertical Laplacian viscosity of 1 $cm^2\ s^{-1}$, the same vertical Laplacian diffusivity A_v = 0.2 $cm^2\ s^{-1}$, and the barotropic mode was solved with the rigid-lid streamfunction method (Bryan 1969).

For each experiment, the model's thermal structure is initialized by running a coarse horizontal resolution, zonally symmetric, case for 9000 yr. This initialization phase employed a horizontal Laplacian viscosity of 2×10^9 $cm^2\ s^{-1}$, zero horizontal diffusion, and the quicker advection scheme. The resulting solution, which is essentially time independent, is then interpolated to various fine horizontal resolution grids without changing the vertical resolution. On this fine grid, the vertical viscosity and diffusivity are held fixed from the coarse grid, but the horizontal Laplacian viscosity and zero diffusivity are each changed to nonzero biharmonic operators. Given the large initial isopycnal slopes, the solution is baroclinically unstable. Hence, a bit of noise added to the fine-grid resolution temperature field will generally induce a transition to a zonally asymmetric state consisting of baroclinic eddies. In turn, the initially steep isopycnals tend to relax as APE is transferred to kinetic energy.

With the exception of two cases, all experiments reported in the following used the quicker advection scheme. Integration of the model proceeded for 850 days (except for one case that ran for only 400 days), and the effective diapycnal diffusion was assessed at selected points within this period. Since each of the experiments are run independently, and because the solutions are turbulent, the states for which effective diffusivities are computed will differ in details between the cases. This difference will generally create some sensitivity to the reported diffusivities. However, extensive analysis of the experiments has indicated that the qualitative results are robust, and the quantitative results are only modestly dependent on these details.

b. General features of a solution

In general, a solution evolves from the initial condition taken from the coarse experiment, where variance is concentrated at the large scales and there is a large reservoir of APE, to an intermediate stage in which linearly unstable zonal baroclinic waves evolve into fully nonlinear breaking waves, to a final stage in which the flow is dominated by large-scale predominantly barotropic structures.

These stages are illustrated in Fig. 10 for a case that has a $\frac{1}{6}° \times 25$ m grid, a horizontal biharmonic viscosity of 10^{19} $cm^4\ s^{-1}$, and a horizontal biharmonic diffusivity of 10^{18} $cm^4\ s^{-1}$. The left column shows a meridional-vertical slice of the temperature field in the middle of the channel. Note the tendency by day 400 for the solution to have intermittent regions of relatively flat isotherms separated by steeper ones. This character reflects the transfer of APE to mean and eddy kinetic energy by the breaking baroclinic waves.

The middle column shows the temperature field at model level 3, which is at 62.5-m depth, over the latitudinal range 20°–40°S. The solution at day 250 corresponds to a time near the end of the linear unstable growth phase and beginning of the fully nonlinear phase. The most unstable linear mode is seen to have a zonal wavelength of roughly 2°–3° at 30°S, which can be represented even by the coarsest grids used. Day 400 shows a fully nonlinear regime with breaking waves, strong gradients, and a concomitant vigorous amount of eddy stirring. It is this period of the experiment that provides the most extreme test of the numerics, and so it will form the focus of the subsequent analysis. Day 850 shows the solution with variance mostly near the largest scales. By this time, the solution has reached the conclusion of the baroclinic to barotropic transition (Rhines 1977; Salmon 1998), with some intermittent smaller-scale structures arising from the continual APE recharging from the surface thermal restoring. Note that horizontal slices at all model depths show a similar evolution. The third column shows the corresponding relative vorticity, whose evolution largely reflects that seen in the horizontal temperature field.

c. Varying the horizontal grid resolution

Varying the horizontal resolution without changing the subgrid-scale parameters allows for an assessment of the effects that grid resolution has on the amount of spurious diapycnal mixing. For this purpose, we performed two suites of experiments: suite A, consisting of eight cases that have resolutions from $\frac{1}{2}°$ to $\frac{1}{9}°$, and suite B, consisting of three cases that used $\frac{1}{3}°$, $\frac{1}{6}°$, and $\frac{1}{9}°$. Each case used quicker advection, 10^{18} $cm^4\ s^{-1}$ biharmonic viscosity, and had the same uniform 25-m-thick boxes. The two suites differ only by the horizontal biharmonic diffusivity applied to the temperature field: suite A used 10^{19} $cm^4\ s^{-1}$ and

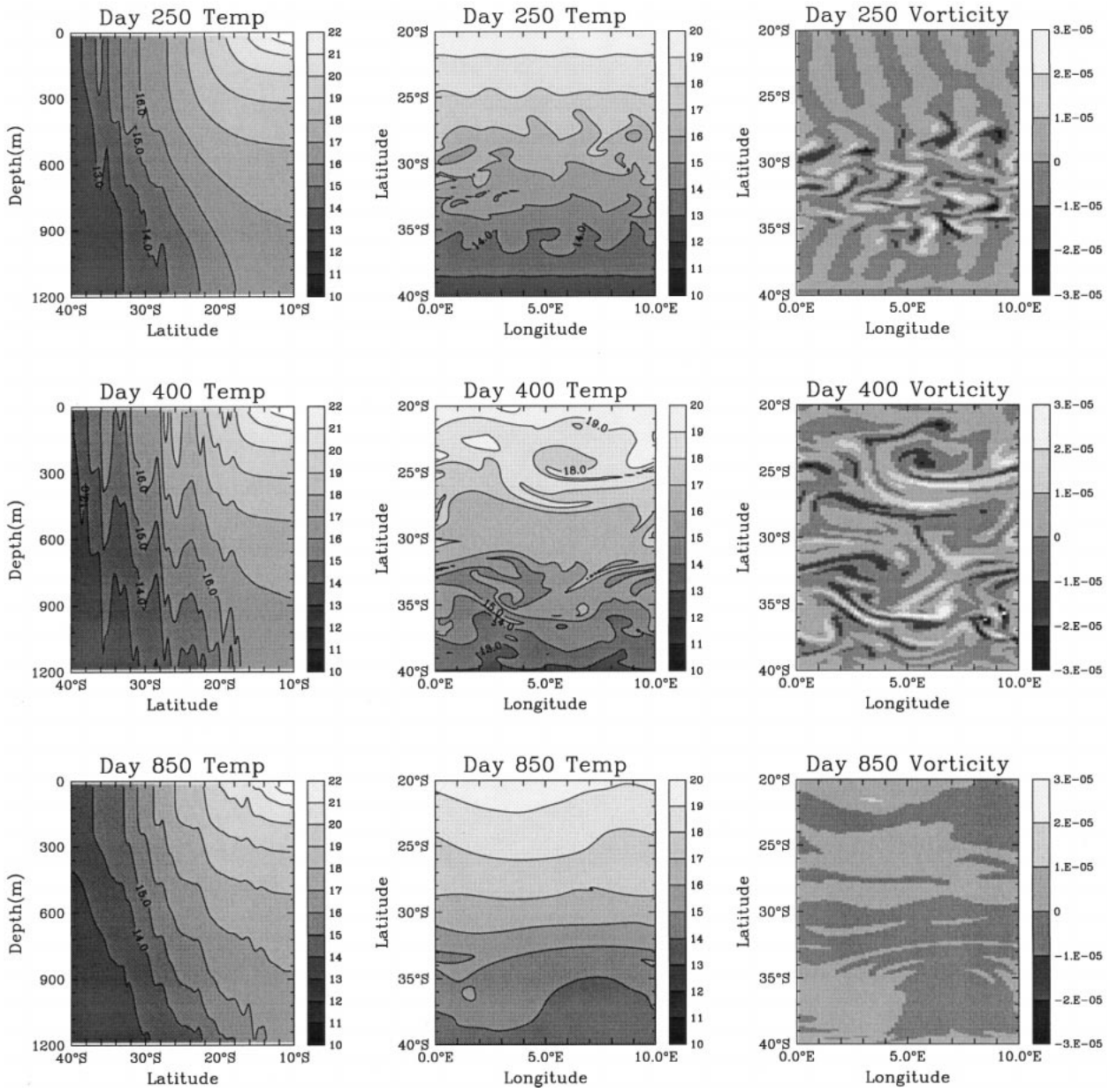

FIG. 10. Representative snapshots from an experiment using a $\frac{1}{6}^\circ \times 25$ m grid, a horizontal biharmonic viscosity of 10^{19} cm^4 s^{-1}, and a horizontal biharmonic diffusivity of 10^{18} cm^4 s^{-1}. Left column from top to bottom: Meridional-vertical snapshots of the temperature field at $\lambda = 5^\circ$ for days 250, 400, and 850. Middle column: Corresponding horizontal snapshot of temperature at level 3 (62.5 m) from 20°S to 40°S. The solution north of 20°S is generally more quiet, as evidenced by the meridional-vertical snapshots. Note the slightly different shading relative to the meridional-vertical snapshots. Right column: Corresponding relative vorticity at level 3 (s^{-1}).

Suite B used 10^{18} cm^4 s^{-1}. We focus on suite B's $\frac{1}{6}^\circ$ experiment as a "standard case."

1) RESOLUTION AND SPECTRA

Figure 11 shows a plot of the zonal temperature variance $\langle T^2 \rangle_x - \langle T \rangle_x^2$ at 62.5-m depth for day 400 in the suite B experiments. In this expression, the angled brackets represent a zonal average. Other depths look similar, but with a general tapering of the power with depth. This plot illustrates that the magnitude of the large-scale anomalies tends to increase with grid resolution, which in turn is associated with a more complete representation of the turbulent transfer of energy to the large scales. Figure 12 shows the corresponding spectral power. Comparison of the these spectra, especially those for the two highest resolution cases, illustrates that when holding the subgrid-scale parameters fixed while increasing the grid resolution, the power at the small scales tends to remain roughly the same, yet the number

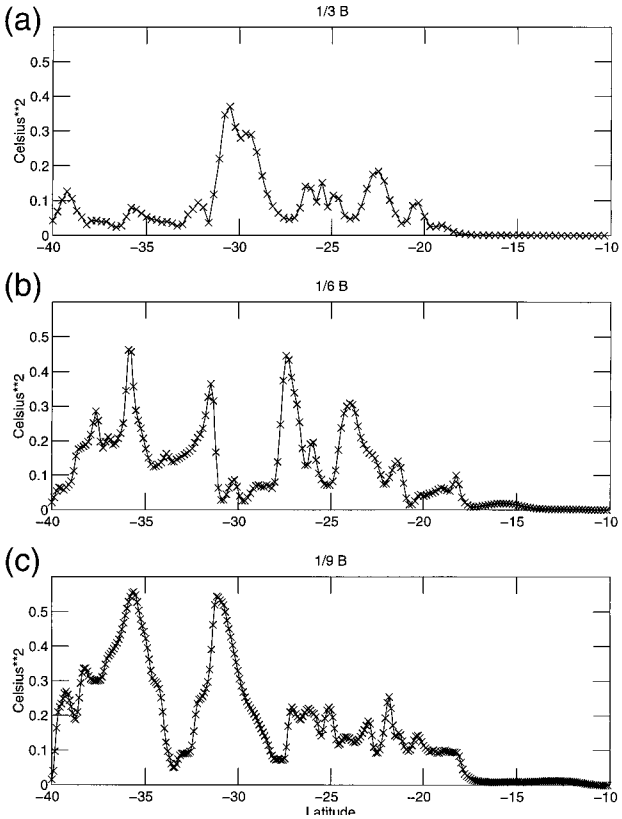

FIG. 11. Zonal temperature variance $\langle T^2 \rangle_x - \langle T \rangle_x^2$ for suite B experiments as a function of latitude at 62.5-m depth and at day 400: (a) $\frac{1}{3}^\circ$ experiment, (b) same plot for the $\frac{1}{6}^\circ$ experiment, (c) same plot for the $\frac{1}{9}^\circ$ experiment.

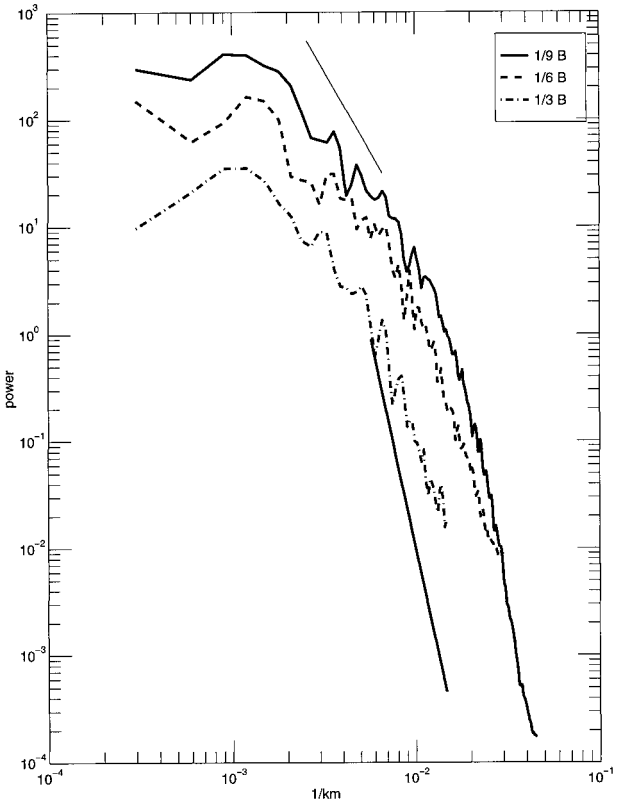

FIG. 12. Power spectrum for the zonal anomalous temperature field from the suite B experiments at day 400. Solid line is for the $\frac{1}{9}^\circ$ experiment, the dashed line is for the $\frac{1}{6}^\circ$ experiment, and the dot-dashed line is for the $\frac{1}{3}^\circ$ experiment. The two solid straight lines denote k^{-3} and k^{-8} behaviors. Note that the lowest wavenumber $1/L$ is the same for each experiment, where $L \approx 3300$ km is the latidudinal extent of the channel, whereas the highest wavenumber $1/\Delta y$ differs because of the varying grid resolution. Also note that an averaged value of Δy for each case is used for purposes of plotting. More general spherical harmonic spectral analysis (e.g., Boer and Shepherd 1983), should lead to qualitatively similar results.

of grid points resolving these structures increases. Note that as the higher wavenumbers are approached, the slope of the spectrum tends to steepen. An exponential fall-off of power at the high wavenumbers is expected for a well-resolved dissipation range. Importantly, there is no significant indication of a flattening of the spectrum at the highest wavenumbers, which would be a strong sign of underdissipation of the grid scales.

2) EFFECTIVE DIFFUSIVITY FOR SUITE B'S $\frac{1}{6}^\circ$ EXPERIMENT

To introduce the results for the effective diapycnal diffusivity κ_{eff}, we first focus on the suite B's $\frac{1}{6}^\circ$ case. For this purpose, Fig. 13 shows its κ_{eff} values at day 400. Figure 13a shows κ_{eff} when using quicker advection, a biharmonic diffusivity of $A_h = 10^{18}$ cm^4 s^{-1}, and a vertical diffusivity of $A_\nu = 0.2$ cm^2 s^{-1}. Recall that these subgrid-scale parameters were used during the experiment when run under the surface restoring. Compared to the small background values realized with $A_\nu = 0.2$ cm^2 s^{-1} alone, one concludes that the κ_{eff} is roughly 10–20 times larger than physically realistic.

Diagnosis of the κ_{eff} values at day 850, which again is during the latter portion of the experiment in which the variability is localized to the large scales, reveals much smaller values (not shown), which are all near the $A_\nu = 0.2$ cm^2 s^{-1} background. For the purpose of exposing the difficulties inherent in realizing more vigorous, and interesting, eddy fields, we therefore focus on the following in day 400 results.

It is of interest to establish the linearity of the different contributions to the κ_{eff} values seen in the Fig. 13a. To do so, we successively turned off various transport processes. As shown in Fig. 13c, without explicit vertical diffusion, the effective diapycnal diffusivity reduces by an amount corresponding to the small values present just with vertical diffusivity alone. Figure 13e shows κ_{eff} diagnosed with just horizontal biharmonic diffusivity. It becomes large with depth, consistent with horizontal diffusion contributing more diapycnal mixing across steep outcropping layers. Note that the horizontal biharmonic diffusion in the channel contributes much less diapycnal mixing than horizontal Laplacian diffusion in the sector (cf. Figs. 5 and

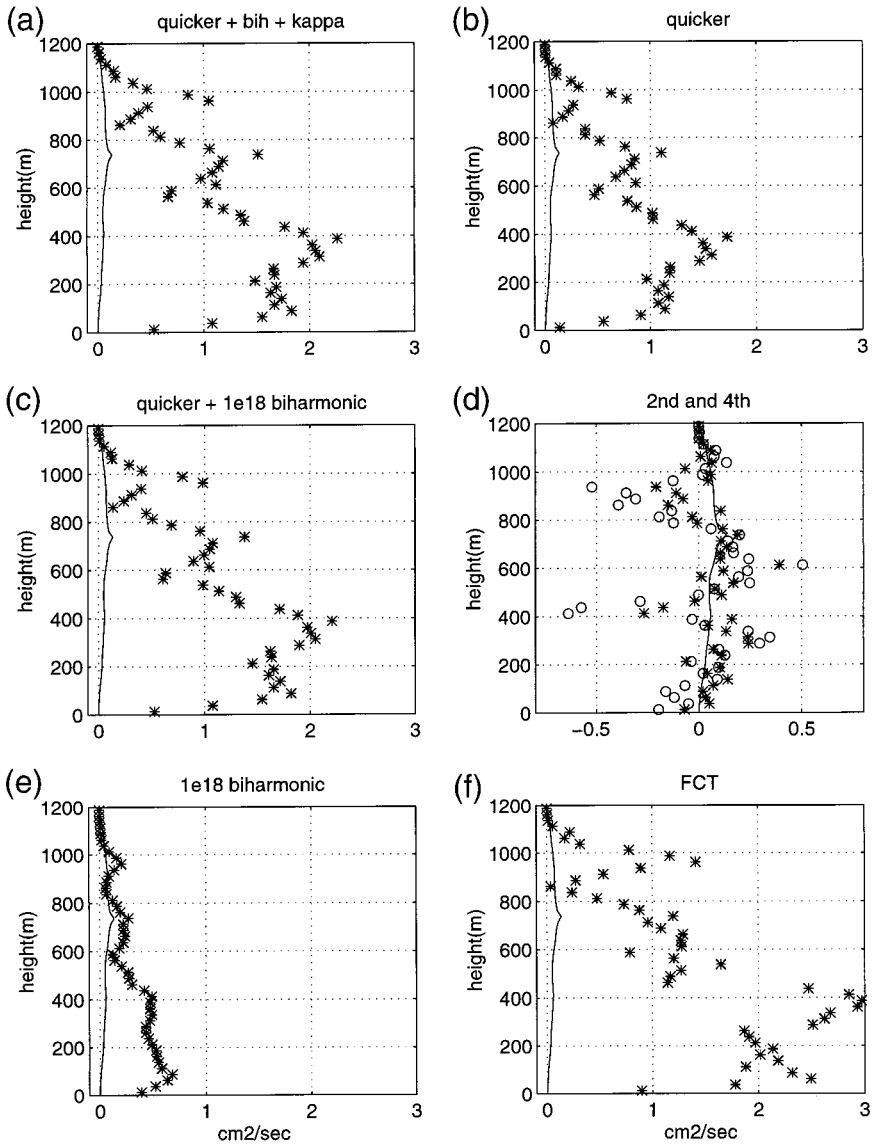

FIG. 13. Effective diffusivities κ_{eff} as a function of height from the ocean bottom for suite B's $\frac{1}{6}^\circ$ experiment at day 400. (a) Quicker, horizontal biharmonic diffusivity of $A_h = 10^{18}$ cm^4 s^{-1}, and vertical diffusion $A_v = 0.2$ cm^2 s^{-1}. (c) Quicker and biharmonic diffusivity. (e) Just horizontal biharmonic diffusion. (b) Just quicker advection. (d) Second-order centered differences (○) and a separate case with fourth-order advection (*). (f) FCT. The solid line in each panel corresponds to the effective diapycnal diffusivity associated with a vertical diffusivity of $A_v = 0.2$ cm^2 s^{-1}.

13). The differences can be attributed to the relatively smaller area of steep isopycnals at day 400 in the eddying channel than at year 5000 in the laminar sector, as well as the added scale selectivity of the biharmonic operator.[4] Figure 13b shows the result with just quicker advection, whose values are largely positive. A linear sum of the three κ_{eff} values yields a κ_{eff} quite close to that diagnosed when all three processes are run together. Thus, the different processes add in a linear fashion to the total effective diffusivity. Importantly, we see that the total effective diffusivity reported in Fig. 13a is dominated by the contribution from quicker advection: the horizontal biharmonic diffusion contributes about three times less than quicker, and the vertical diffusion contributes about ten times less.

Figure 13d shows results from the second-order and fourth-order advection schemes. There are both positive and negative effective diffusivities. In general, the amount of spurious mixing realized with the fourth-

[4] As noted by Roberts and Marshall (1998), additional diapycnal mixing is associated with horizontal biharmonic diffusion acting in western boundary regions in sector models. This source is missing in flat-bottomed zonal channel models.

order scheme is smaller than with the second-order scheme, sometimes by as much as a factor of two. A technical question concerns how accurate the effective diffusivities are for these schemes given that they were not used during the integration to day 400. To address this question, we ran another experiment for 800 days, which used second-order advection. A diagnosis of the spurious mixing associated with second-order advection in this new experiment shows somewhat larger values than those shown in Fig. 13. An explanation can be found by noting that with the same subgrid-scale parameters, the conservative second-order scheme will allow more power to build up at the grid scale than the dissipative quicker scheme, hence increasing the tendency for dispersion errors and so raising the magnitude of $\kappa_{\rm eff}$.

Figure 13f shows the results from FCT. The diffusivity profile is similar to the quicker results, albeit with somewhat larger values. We diagnosed the spurious mixing from the upwind scheme as well, and the results (not shown) are roughly an order of magnitude larger than the FCT scheme. In a manner similar to the second-order experiment discussed above, we ran an experiment to test the accuracy of the effective diffusivities for the FCT scheme shown in Fig. 13. A diagnosis of the FCT diffusivities from this new case are consistent with those in Fig. 13.

3) SCALING WITH HORIZONTAL RESOLUTION

The central question that suites A and B are aimed at addressing is how the spurious mixing is affected by changes in the horizontal grid resolution. The spectral analysis given previously suggests that the $\frac{1}{3}^\circ$ case underresolves its flow structures at day 400, the $\frac{1}{6}^\circ$ case is adequate, and the $\frac{1}{9}^\circ$ case is very well resolved. Figure 14 provides evidence that so far as reducing the spurious mixing to levels below a background level corresponding to $A_v = 0.2$ cm^2 s^{-1}, even the $\frac{1}{9}^\circ$ solution is inadequate. In this figure, we report the effective diapycnal diffusivities corresponding to the quicker advection scheme alone. The results from other schemes are consistent with those seen in Fig. 13.

Notice that the effective diffusivities from suite B experiments are generally larger than the suite A experiments. The reason is because with larger biharmonic diffusivities, suite A experiments require less dissipation from the quicker advection scheme to absorb the variance cascade. In turn, the effective diffusivities associated with the biharmonic scheme (not shown) are roughly 4–6 times larger for suite A than suite B. Hence, there is a trade-off between the effective diapycnal mixing associated with the horizontal biharmonic diffusion and dissipation coming from the advection scheme.

Although the effective diffusivities are depth dependent, it is useful to summarize the results with a single number. For this purpose, we form the vertically averaged quantity

$$\kappa_{\rm avg} = \frac{\int dz^* \, [|\kappa_{\rm eff}(z^*)| - \kappa^B_{\rm eff}(z^*)]}{\int dz^*}, \qquad (6)$$

where $\kappa^B_{\rm eff} \geq 0$ is a background effective diffusivity arising from $A_v = 0.2$ cm^2 s^{-1} vertical diffusion. The absolute value sign counts negative and positive $\kappa_{\rm eff}$ values equally. Values for $\kappa_{\rm avg}$ are reported in Fig. 15 for the quicker advection scheme as derived from suites A and B. Generally, the $\kappa_{\rm avg}$ values are positive, which indicates larger amounts of effective diapycnal mixing than that associated with the $A_v = 0.2$ cm^2 s^{-1} background.

Also plotted in Fig. 15 is a straight line corresponding to a quadratic scaling of $\kappa_{\rm avg}$ with the grid resolution: $\kappa_{\rm avg} \propto \Delta\lambda^2$. Although this scaling is rough, it does provide a sense as to how fast the spurious mixing is reduced with increased grid resolution. The quadratic scaling is consistent with the quadratic order of the quicker advection scheme. Although in general a quadratic scaling is quite reasonable, the difficulty with reducing the spurious mixing in these experiments stems from the constant multiplier, which sets the overall scale of the effective diapycnal diffusivity. Note that the quadratic scaling appears less relevant for the $\frac{1}{2}^\circ$ and $\frac{1}{3}^\circ$ grids. The reason is that for these coarse experiments, the eddy activity is relatively weak and so the spurious mixing is tapering off.

d. Varying the vertical grid resolution

To examine the effects of vertical resolution on the effective diapycnal mixing, we performed two new experiments using the same configuration as the standard suite B's $\frac{1}{6}^\circ$ case discussed above, yet with less vertical resolution. The three experiments then have $\Delta z = 50$ m, $\Delta z = 33.3$ m, and $\Delta z = 25$ m. Figure 16 documents the effective diapycnal diffusivity associated with quicker advection plus horizontal biharmonic diffusion plus vertical diffusion. It also shows results from quicker advection alone. All results are taken at day 400 of the three experiments. We see that the advection scheme contributes the most to the total amount of effective mixing. The averaged diffusivity defined by Eq. (6) gives values of 0.90 cm^2 s^{-1}, 0.95 cm^2 s^{-1}, and 0.70 cm^2 s$^-$ for the 24-, 36-, and 48-level experiments, respectively. The results indicate some sensitivity to vertical resolution, with higher resolution reducing the spurious mixing. We expect that in the presence of strong vertical velocities associated with Ekman pumping, topography, and/or boundaries, the sensitivity to vertical resolution, especially in the thermocline, should be ex-

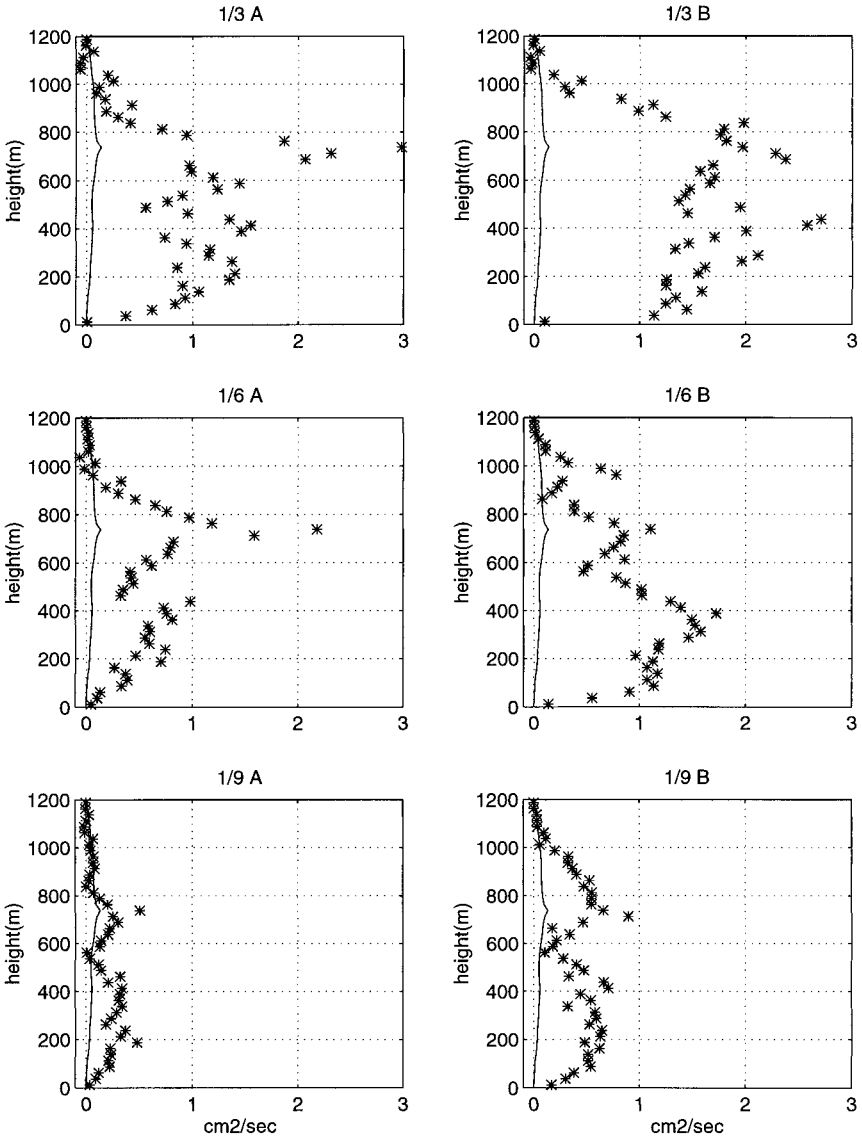

FIG. 14. Effective diapycnal diffusivities associated with quicker advection for suite A (left column; biharmonic diffusivity 10^{19} cm^4 s^{-1}) and suite B (right column; biharmonic diffusivity 10^{18} cm^4 s^{-1}). The solid line in each panel is the effective diffusivity arising from a case with vertical diffusivity of $A_v = 0.2$ cm^2 s^{-1}. Grid resolution increases from $\frac{1}{3}^\circ$, $\frac{1}{6}^\circ$, and $\frac{1}{9}^\circ$ moving from top to bottom in each column.

hibited even more prominently than in this flat-bottomed channel model.

e. Varying the horizontal biharmonic viscosity

As a final suite, we consider the sensitivity of spurious diapycnal mixing to the horizontal biharmonic viscosity. The idea is that by changing the viscosity, we will reduce the power at the grid scale in the velocity field and hence, indirectly, reduce the tendency for dispersion errors to contribute to the spurious tracer mixing. Each experiment used a rather small horizontal biharmonic diffusivity of 10^{17} cm^4 s^{-1}. This value, as seen below, renders the spurious mixing from horizontal diffusion adequately small, and does not appear to compromise the integrity of the temperature field, at least for the cases with larger viscosity and hence smaller velocities.

Figure 17 shows the effective diffusivities for these three experiments. Shown in the left column are the total diffusivities associated with quicker advection, horizontal biharmonic diffusion, and vertical diffusion, and the right column shows results for just quicker advection. Notice that the results in both columns are quite close, hence indicating that the horizontal biharmonic diffusivity of 10^{17} cm^4 s^{-1} is negligible so far as spurious mixing is concerned for these channel experiments. Also

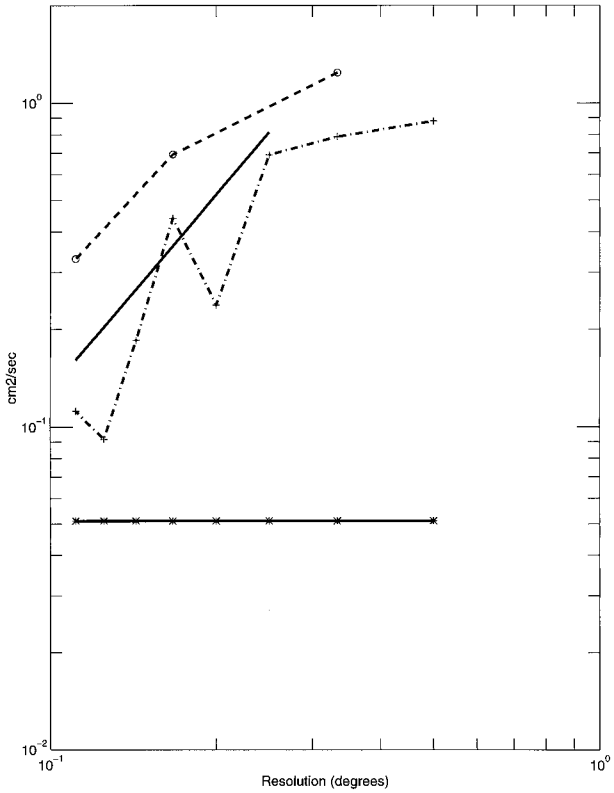

FIG. 15. A log–log plot of the vertically averaged effective diffusivities κ_{avg}, according to Eq. (6), for the quicker advection scheme taken from day 400 of various experiments. The top dashed line corresponds to suite B and the lower dot-dashed line to suite A. The straight slanted solid line corresponds to a scaling of κ_{avg} as $(\Delta\lambda)^2$. The horizontal solid line corresponds to the background effective diapycnal diffusivity arising from vertical diffusion with $A_v = 0.2$ cm^2 s^{-1}.

notice the rather strong dependence of the spurious mixing on the viscosity. The value of κ_{avg} for the total mixing is 1.2 cm^2 s^{-1}, 0.14 cm^2 s^{-1}, and -0.02 cm^2 s^{-1}, respectively.

The question is whether we have sacrificed too much of the eddy activity in order to reduce the spurious mixing. First, note that the maximum total kinetic energy per unit mass of the three cases is 625 cm^2 s^{-2}, 190 cm^2 s^{-2}, and 40 cm^2 s^{-2}, which is expected since viscosity directly dissipates kinetic energy. Figure 18 shows a snapshot at day 400 of the horizontal temperature field for the three experiments. This picture reveals why the spurious mixing in the highly viscous case is so small—the solution has yet to go nonlinear by day 400, whereas the other two cases are well within the nonlinear turbulent regime. The averaged effective diffusivities for the lower viscosity cases represent an eight-fold reduction in the spurious mixing associated with the three-fold reduction in total kinetic energy. This result indicates the utility of tuning the horizontal viscosity along with the diffusivity and advection scheme for the purpose of reducing the overall effective diapycnal mixing.

7. Discussion and conclusions

a. Comments on topography and ''digging''

Recent advances in coarse-resolution *z*-level models associated with the realization of isopycnal processes have allowed for the reduction of horizontal background diffusion (e.g., Gent and McWilliams 1990; Griffies et al. 1998; Griffies 1998). With the older numerics, this diffusion acted to stabilize the models, yet the amounts required tended to introduce unphysical amounts of diapycnal mixing. As sometimes occurs in ocean modeling, the use of horizontal background diffusion often masked problems other than those related to isopycnal processes. Notably, removing background diffusion can expose the solution to ''digging,'' which is the creation of extreme water mass properties at rough side and bottom boundaries. Digging arises from advective dispersion errors, and it is most often, though not solely, found near topography with strong grid-scale variations. One may speculate that if topography were instead constructed with variations only at longer wavelengths, then the amount of digging conceivably would be reduced. The advent of partial bottom cells (Pacanowski and Gnanadesikan 1998), or the more general shaved cells (Adcroft et al. 1997), reduces the amplitude of these grid-scale variations, and it has been shown in two-dimensional examples to reduce dispersive errors. The hope is that such improvements will translate into less digging in realistic three-dimensional models.

Relatedly, it is interesting to highlight that measurements (Polzin et al. 1997) suggest that mixing in the ocean is increased near rough topography. Consequently, mixing associated with a dissipative advection scheme, which necessarily kicks in near rough topography, is arguably adding mixing where the ocean also has strong mixing. However, it is our contention that an explicit parameterization of boundary mixing, such as that used by Blumberg and Mellor (1987) in sigma-models, or advocated by Beckmann and Döscher (1997) or Killworth and Edwards (1997) for level models, combined with a better level coordinate representation of topography through partial or shaved cells, is more physically satisfying since it allows the modeler to have direct knowledge and control over the levels of mixing.

b. Summary and conclusions

The central purpose of this paper was to articulate issues that relate to the spurious mixing of density associated with the numerical representation of advection in *z*-coordinate ocean models. Ideally, advection should not alter the water mass census, and it is in this manner that advection is an adiabatic transport process. Recent measurements provide compelling evidence that in the

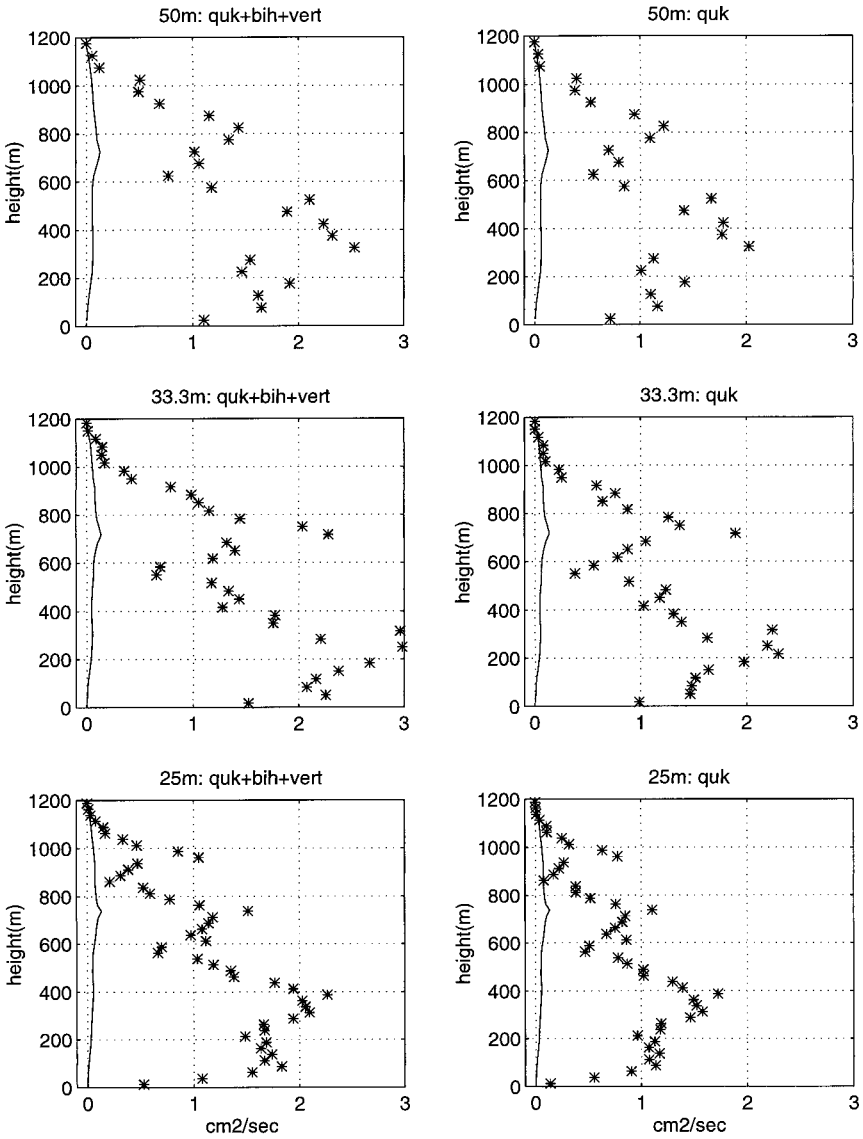

FIG. 16. Effective diapycnal diffusivities for the vertical resolution suite. The left column is the total spurious mixing for quicker advection, horizontal biharmonic diffusion with $A_{bih} = 10^{18}$ cm^4 s^{-1}, and vertical diffusion with $A_v = 0.2$ cm^2 s^{-1}. The right column is for quicker advection alone. Upper panels: 50-m-thick boxes (24 levels), middle panels: 33.3-m-thick boxes (36 levels), and lower panels: 25-m-thick boxes (48 levels). The solid line in each panel is the effective diapycnal diffusivity from a vertical diffusivity of $A_v = 0.2$ cm^2 s^{-1}.

ocean interior, the levels of diapycnal mixing are quite small (Ledwell et al. 1993; Kunze and Sanford 1996). As such, it is important to empirically measure the levels of diapycnal mixing in numerical models to determine to what extent they respect the ocean measurements.

The key problem with *z*-level (and by analogy, sigma coordinate) models that underlies the points raised by this study is that their advective fluxes are not explicitly constrained to preserve adiabaticity. Rather, they must rely on numerical convergence, which requires an adequate resolution of the admitted flow structures. If not carefully tuned, the results in this paper indicate that models can manifest unphysically large amounts of diapycnal mixing due to numerical truncation errors. In contrast, isopycnal-layer models, within the confines of their specified layers, build the adiabaticity constraint into the numerics in a fundamental manner, and so do not suffer from these problems.

We introduced some of the basic problems with advection in *z*-level ocean models through examining a one-dimensional advection-convection model of a seasonally forced thermocline. The point emphasized was simple: advection dispersion errors, when coupled to convection, can add nonlocal and irreversible spurious

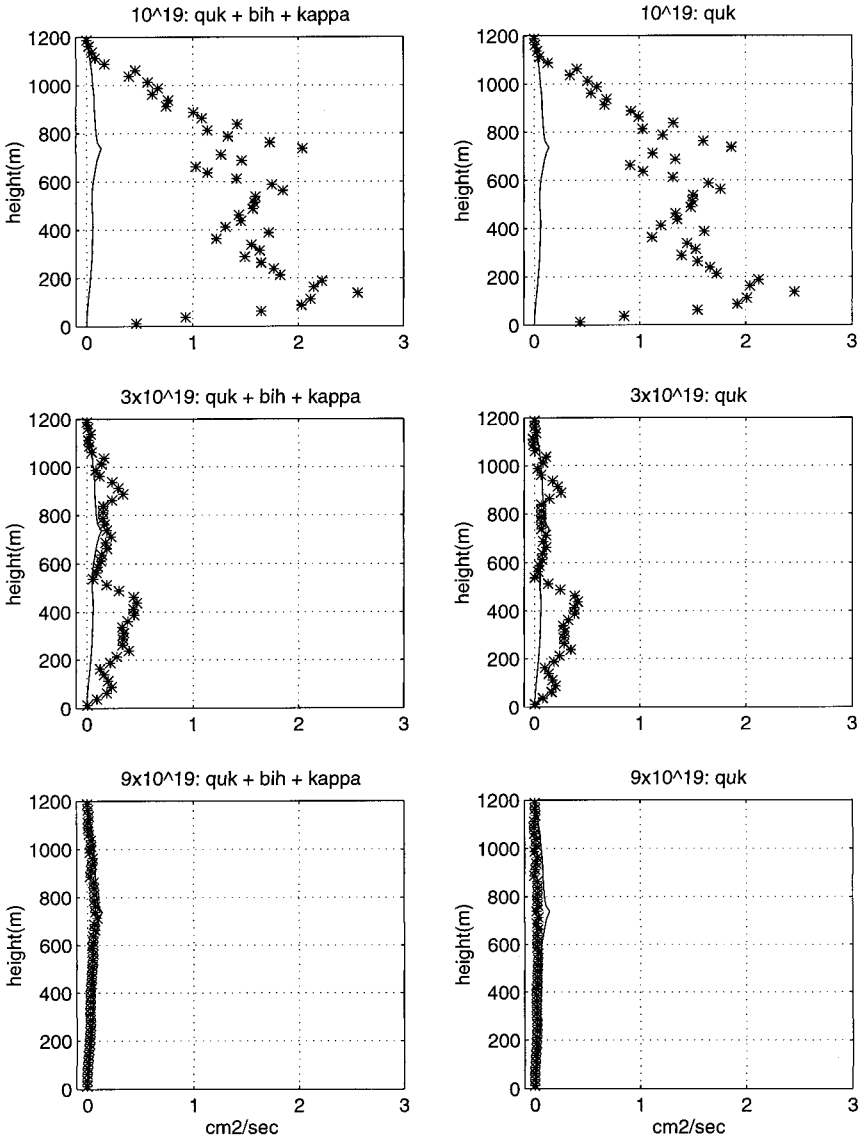

FIG. 17. Left column: effective diapycnal diffusivities associated with quicker advection, horizontal biharmonic diffusion with coefficient 10^{17} cm^4 s^{-1}, and vertical Laplacian diffusion with $A_v = 0.2$ cm^2 s^{-1}. The three experiments differ in their values of horizontal biharmonic viscosity. Upper panels: viscosity $= 10^{19}$ cm^4 s^{-1}, middle panels: viscosity $= 3 \times 10^{19}$ cm^4 s^{-1}, and bottom panels: viscosity $= 9 \times 10^{19}$ cm^4 s^{-1}. Right column: Corresponding effective diapycnal diffusivities associated with quicker advection alone. The solid line in each panel is the effective diapycnal diffusivity arising from a vertical diffusivity of $A_v = 0.2$ cm^2 s^{-1}.

numerical processes, which affect the evolution of water masses. The accumulated effects from these processes tend to artificially enhance the difference between the dense abyssal waters and lighter surface waters.

After the one-dimensional example, we moved into our main line of analysis, which was the quantification of effective levels of diapycnal mixing occurring in three-dimensional z-level ocean models. Our tool for this purpose was based on the work of Winters et al. (1995) and Winters and D'Asaro (1996). They introduced the notion of an effective diapycnal diffusivity, which summarizes the amount of mixing across density surfaces. As such, the effective diffusivity is directly representative of the rate of water mass transformation. Crucially, this diffusivity is quite easy to compute in z-models, regardless of the subgrid-scale parameterizations or advection schemes. Hence, it provides a valuable empirical tool for use in determining the levels of diapycnal mixing present in a model.

Although a total of five advection schemes were examined here, the FCT (flux corrected transport) and quicker schemes were the main focus of this study. Our

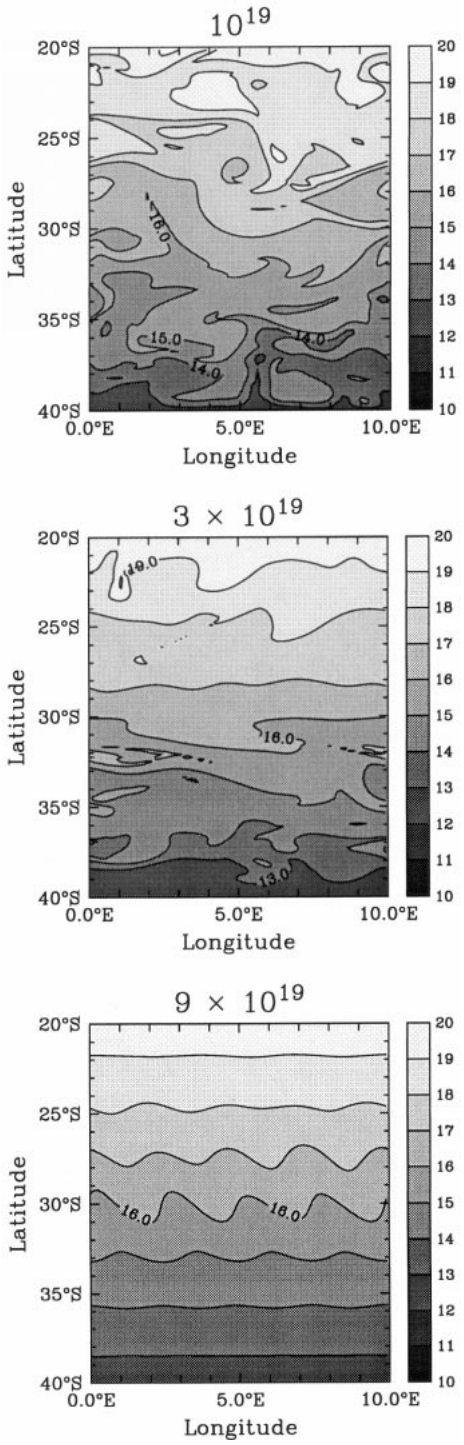

FIG. 18. Horizontal snapshots of temperature fields at day 400 for the viscosity suite of experiments. Upper panel: viscosity = 10^{19} cm^4 s^{-1}, middle panel: viscosity = 3×10^{19} cm^4 s^{-1}, and lower panel: viscosity = 9×10^{19} cm^4 s^{-1}.

motivation for this focus stems from the utility that these schemes have exhibited for large-scale ocean modeling (e.g., Gerdes et al. 1991; Farrow and Stevens 1995; Holland et al. 1998).

To illustrate the issues related to spurious mixing, we focused on two idealized model configurations: a coarse-resolution sector and a fine-resolution channel. In the coarse-resolution sector with underresolved flow scales, second-order centered advection exhibited nontrivial dispersive errors that translated into unphysical flow structures. The same experiment run with FCT showed a more reasonable solution, but at the cost of adding spurious diapycnal mixing from its upwind component. The result was a spurious diapycnal mixing corresponding to a vertical diffusivity $A_v \approx 0.3$–0.4 cm^2 s^{-1}, which is two to three times too large. An increase in horizontal resolution *without* changing the subgrid-scale parameters, thus resolving the model's western boundary current with at least two grid points, brought this spurious mixing down to negligible values.

This result is consistent with other coarse-resolution z-model studies that show close agreement with geostrophic scaling relations as the vertical diffusivity is scaled toward zero (e.g., Samelson and Vallis 1997; Park and Bryan 1999), as well as the results from Hirst and McDougall (1998), who investigated the amount of dianeutral mixing occurring in a particular global ocean model and found it to be small. We conclude, therefore, that coarse z-models with reasonably well-resolved flow structures typically maintain a negligible amount of spurious mixing. However, when allowing unresolved flow features, the model will tend to contain unphysically large amount of spurious diapycnal mixing, and this mixing predominantly occurs in dynamically active and important regions such as western boundary currents.

In the presence of eddies, modelers typically aim to realize the following three properties in a solution: 1) energetic eddies with little dissipation at the large scales, 2) adequate dissipation near the grid scale to provide a sink for the enstrophy and variance cascades, and 3) small amounts of spurious diapycnal mixing. For the present study, we focused on determining when the third goal is satisfied as defined by our effective diapycnal diffusion diagnostic. The first and second goals were defined only so far as the solution realized a nontrivial eddying field, which was reasonably well dissipated at the grid scale.

Results with a fine-resolution channel model show that satisfying these three goals involves the interplay between advection schemes, tracer and momentum dissipation, and grid resolution. In particular, our presentation focused on the quicker advection scheme. Quicker showed an approximate quadratic scaling between grid resolution and effective diapycnal diffusivity; a scaling consistent with the scheme's truncation errors. The overall scale setting the magnitude of the effective diapycnal diffusivity, however, was quite large, thus making it necessary to go to relatively high grid resolution before

reducing the diffusivity to near acceptable values. If one sacrifices some eddy energy by adding more biharmonic viscosity, the spurious mixing can be significantly reduced but at the cost of reducing the kinetic energy.

In conclusion, the results from the eddy permitting model indicate that to realize physically negligible levels of spurious mixing in the presence of vigorous eddy activity requires a substantially better resolution of the dissipation range than prompted by goals 1) and 2) alone. This result is highly relevant given the aim to construct realistic eddy-permitting z-coordinate climate models, which are to be run for centuries or longer. Quite simply, the current suite of numerical schemes needs to be improved in order to maintain a realistically small amount of spurious mixing in these models.

As an outgrowth of this research with the eddy permitting model, we are currently pursuing alternative numerical schemes in hopes of more readily satisfying goals 1, 2, and 3. One intriguing new scheme involves the adiabatic biharmonic dissipation operator of Roberts and Marshall (1998). In tests with a z-level wind-driven eddying sector model, they showed how their operator reduced the overall diapycnal mixing compared to horizontal biharmonic diffusion. Another promising approach is to employ dissipative advection schemes combined with high-order accurate numerics. For example, as seen in this paper, the pseudo-fourth-order centered scheme reduced the amount of dispersion errors relative to the second-order scheme. If used within an FCT-like approach, or perhaps in the manner proposed by Shchepetkin and McWilliams (1998), then the overall amount of spurious mixing might be reduced relative to that engendered with MOM's second-order FCT scheme.

In closing, we note that the results of this study do not lead us to advocate the universal use of a particular advection scheme. Even upwind has its use for certain systems [e.g., parameterized bottom boundary layers or idealized box models such as Stommel (1961)]. The innumerable regimes of ocean flow, and the corresponding model applications, preclude such a position. Rather, we do advocate that ocean modelers and numerical analysts consider the amount of spurious diapycnal mixing associated with the representation of tracer transport, be it realized through advection or some explicit dissipation operator. When doing so, the choices made for subgridscale parameters and grid resolution are more subtle than when focusing just on more traditional considerations. There are many numerically stable models with respectably smooth solutions that also have unphysically large amounts of spurious diapycnal mixing. When integrated over climatologically relevant timescales (order of centuries), which involve thousands of advective timescales, this mixing could seriously compromise the physical integrity of the solution.

Acknowledgments. We wish to thank Jerry Mahlman for useful discussions, motivation, and his fourth-order tracer advection scheme. We also thank Anand Gnanadesikan, Isaac Held, Young-Gyu Park, Geoffrey Vallis, and Mike Winton for useful discussions and comments on drafts of this paper, and Robbie Toggweiler and Bonnie Samuels for testing some of the ideas here in their global ocean model. Finally, the comments of the two anonymous reviewers are greatly appreciated.

APPENDIX A

The Accuracy of Second-Order Advection

For second-order centered differences, the discrete approximation for the first derivative of a tracer is given by

$$\frac{T_{i+1} - T_{i-1}}{2\Delta x} = T_x + \frac{(\Delta x)^2}{3!} T_{xxx} + \frac{(\Delta x)^4}{5!} T_{xxxxx} + O(\Delta x^6). \quad \text{(A1)}$$

If the tracer has spatial variability in the form of a wave $T = T_o \sin(kx)$, then the discrete first derivative of the wave takes the form

$$\frac{T_{i+1} - T_{i-1}}{2\Delta x} = T_o k \cos(kx) \left[\frac{\sin(k\Delta x)}{k\Delta x} \right]. \quad \text{(A2)}$$

The exact result for the first derivative is $T_x = T_o k \cos(kx)$. The truncation error function $[\sin(k\Delta x)]/(k\Delta x)$ approaches unity as $k\Delta x$ gets smaller, in which case the discrete grid better resolves the given wave and hence the centered difference better approximates the first derivative. The smallest wave that can be placed on a discrete grid has wavelength $2\Delta x$, and a corresponding wavenumber $k = \pi/\Delta x$. This wave is not resolvable using centered differences, since the truncation error function vanishes whereas the exact first derivative is $T_o(\pi/\Delta x) \cos(\pi x/\Delta x)$. The next smallest wave that can be placed on the grid has wavelength $3\Delta x$, and the discrete approximation to the first derivative of this wave is given by $T_x [\sin(2\pi/3)](3/2\pi) \approx 0.41 T_x$. Here $8\Delta x$ is the smallest wave whose first derivative is better than 90% accurate using the centered approximation.

Shchepetkin and McWilliams (1998) provide a more thorough analysis of these issues.

APPENDIX B

Effective Diffusivity Calculation Details

The purpose of this appendix is to document the various assumptions made in the diagnosis of the effective diapycnal diffusivity for the MOM experiments.

a. The sorted density profile

The reference density profile is obtained by sorting the $N = N_x \times N_y \times N_z$ grid boxes appearing in the three-dimensional model. For the standard sector model, $N = 25 \times 25 \times 18 = 11\,250$, and for the $\frac{1}{6}^\circ \times 48$

channel model, $N = 60 \times 202 \times 48 = 581\,760$. A rapid sorting routine is readily found in Press et al. (1992). Information regarding both the density and volume of each water parcel is kept during the sort. The volume of the parcel, as well as the model's horizontal cross-sectional area A, are needed to determine the sorted height z^*. The sorted density is then interpolated onto fixed vertical levels using a monotonic piecewise cubic Hermite interpolation. The result is a sorted density profile that generally contains a significant amount of small-scale structure that has the appearance of many small steps. Such steps arise from the sorting map finely interleaving the horizontal and vertical stratification of the unsorted fluid. As seen below, to evaluate the effective diapycnal diffusivity, it is necessary to divide the flux of sorted density by the vertical gradient of the sorted density. The presence of these steps in the sorted density profile renders this calculation extremely noisy.

An alternate procedure was employed, based on the following observation: the best resolution of horizontally uniform density layers that can be realized in a discrete three-dimensional model is N_z, not $N_xN_yN_z$. Therefore, before computing the flux and vertical gradient of the sorted fluid, a layer average, or equivalently a vertical average over regions of z^*, was performed on the sorted fluid. Such an average reduces the vertical resolution to the N_z points used in the discrete model and acts to smooth out the fine vertical steps. This approach can be likened to the smoothing of density into N_z density classes as done in an isopycnal-layer model. The effective diffusivities resulting from this averaging possess much more statistical significance than the unaveraged results. All subsequent reference to the sorted density refers to this layer averaged density, and the vertical resolution Δz^* is identical to the Δz used in the three-dimensional model.

b. The flux and diffusivity

Recall that the goal is to diagnose the flux of sorted density and the effective diapycnal diffusivity, given the time tendency for the sorted density. To do so, a discretization of the sorted fluid's diffusion equation must be assumed. In this paper, the same difference operators that are used in MOM's diffusion equation acting on the unsorted fluid are employed for the sorted fluid.

The diffusive flux of the sorted density [identical to the diapycnal flux F^ρ defined by Eq. (1)] is given by

$$F^\rho(z^*, t) = -\kappa_{\text{eff}}(z^*, t)\partial_{z^*}\rho_{\text{ref}}(z^*, t). \quad \text{(B1)}$$

This flux is defined at the top face of a density cell whose center is at z^*, and the effective diffusivity is defined there as well. The diffusion operator at the lattice point z^*, which is constructed as the convergence of the diffusive flux across a density grid cell, takes the discrete form

$$-\partial_{z^*}F^\rho(z^*, t) \approx -\left[\frac{F^\rho(z^* + \Delta z^*, t - \Delta t) - F^\rho(z^*, t - \Delta t)}{\Delta z^*}\right]. \quad \text{(B2)}$$

The time lag provides for a stable discretization of the diffusion equation, and it mimics that used by MOM. Note that Δt is identical to that used for time stepping the unsorted fluid (i.e., every time step is sampled from the unsorted fluid). The discretization of the vertical diffusive flux of sorted density is given by

$$F^\rho(z^*, t) \approx -\kappa_{\text{eff}}(z^*, t)\left[\frac{\rho_{\text{ref}}(z^* + \Delta z^*, t) - \rho_{\text{ref}}(z^*, t)}{\Delta z^*}\right], \quad \text{(B3)}$$

and the time derivative is approximated using a leapfrog step:

$$\partial_t\rho_{\text{ref}}(z^*, t) \approx \frac{\rho_{\text{ref}}(z^*, t + \Delta t) - \rho_{\text{ref}}(z^*, t - \Delta t)}{2\Delta t}. \quad \text{(B4)}$$

Piecing these results together yields the expression for the vertical flux at the top of the density cell $z^* + \Delta z^*$

$$F^\rho(z^* + \Delta z^*, t - \Delta t) = F^\rho(z^*, t - \Delta t) - \frac{\Delta z^*}{2\Delta t}[\rho_{\text{ref}}(z^*, t + \Delta t) - \rho_{\text{ref}}(z^*, t - \Delta t)]. \quad \text{(B5)}$$

This flux can be determined starting from the ocean bottom, where it vanishes, and working upward. After diagnosing the flux from the tendency, the effective diffusivity is diagnosed from

$$\kappa_{\text{eff}}(z^*, t) = -F^\rho(z^*, t)\left[\frac{\Delta z^*}{\rho_{\text{ref}}(z^* + \Delta z^*, t) - \rho_{\text{ref}}(^*z, t)}\right]. \quad \text{(B6)}$$

A minimum vertical stratification of $\partial_{z^*}\rho_{\text{ref}} = 10^{-10}$ g cm^{-4}, corresponding to roughly a 6-h buoyancy period, is used for the calculation in order to avoid excessive errors with computational precision. Such a weak stratification is seen mostly in the deep ocean (e.g., Pickard and Emery 1990, p. 56), and appears only in a few of the deeper levels of the sector model experiments discussed in section 5. For weaker stratification, the effective diffusivity is set to zero.

REFERENCES

Adcroft, A., C. Hill, and J. Marshall, 1997: Representation of topography by shaved cells in a height coordinate ocean model. *Mon. Wea. Rev.*, **125,** 2293–2315.

Beckmann, A., and R. Döscher, 1997: A method for improved representation of dense water spreading over topography in geopotential-coordinate models. *J. Phys. Oceanogr.*, **27,** 581–591.

Bleck, R., C. Rooth, D. Hu, and L. T. Smith, 1992: Salinity-driven thermocline transients in a wind- and thermohaline-forced iso-

pycnic coordinate model of the North Atlantic. *J. Phys. Oceanogr.,* **22,** 1486–1505.
Blumberg, A. F., and G. L. Mellor, 1987: A description of a three-dimensional coastal ocean circulation model. *Three-Dimensional Coastal Ocean Models,* N. Heaps, Ed., Vol. 4, Amer. Geophys. Union, 208 pp.
Boer, G. J., and T. G. Shepherd, 1983: Large-scale two-dimensional turbulence in the atmosphere. *J. Atmos. Sci.,* **40,** 164–184.
Boris, J. P., and D. L. Book, 1973: Flux-corrected transport. Part I: SHASTA: A fluid transport algorithm that works. *J. Comput. Phys.,* **11,** 38–69.
Bryan, F. O., 1987: Parameter sensitivity of primitive equation ocean general circulation models. *J. Phys. Oceanogr.,* **17,** 970–985.
Bryan, K., 1969: A numerical method for the study of the circulation of the World Ocean. *J. Comput. Phys.,* **4,** 347–376.
——, S. Manabe, and R. C. Pacanowski, 1975: A global ocean–atmosphere climate model. Part II: The oceanic circulation. *J. Phys. Oceanogr.,* **5,** 30–46.
Chen, J.-H., 1971: Finite difference methods and the leading edge problem. Ph.D. thesis, Princeton University, 102 pp.
Cox, M. D., and K. Bryan, 1984: A numerical model of the ventilated thermocline. *J. Phys. Oceanogr.,* **14,** 674–687.
Eckart, C., 1948: An analysis of the stirring and mixing processes in incompressible fluids. *J. Mar. Res.,* **VII,** 265–275.
Farrow, D. E., and D. P. Stevens, 1995: A new tracer advection scheme for Bryan and Cox type ocean general circulation models. *J. Phys. Oceanogr.,* **25,** 1731–1741.
Gent, P. R., and J. C. McWilliams, 1990: Isopycnal mixing in ocean circulation models. *J. Phys. Oceanogr.,* **20,** 150–155.
——, F. O. Bryan, G. Danabasoglu, S. C. Doney, W. R. Holland, W. G. Large, and J. C. McWilliams, 1998: The NCAR climate system model global ocean component. *J. Climate,* **11,** 1287–1306.
Gerdes, R., C. Köberle, and J. Willebrand, 1991: The influence of numerical advection schemes on the results of ocean general circulation models. *Climate Dyn.,* **5,** 211–226.
Gregg, M. C., 1987: Diapycnal mixing in the thermocline: A review. *J. Geophys. Res.,* **92,** 5249–5286.
Griffies, S. M., 1998: The Gent–McWilliams skew-flux. *J. Phys. Oceanogr.,* **28,** 831–841.
——, A. Gnanadesikan, R. C. Pacanowski, V. Larichev, J. K. Dukowicz, and R. D. Smith, 1998: Isoneutral diffusion in a *z*-coordinate ocean model. *J. Phys. Oceanogr.,* **28,** 805–830.
Haidvogel, D. B., J. L. Wilkin, and R. E. Young, 1991: A semi-spectral primitive equation ocean circulation model using vertical sigma and orthogonal curvilinear horizontal coordinates. *J. Comput. Phys.,* **94,** 151–185.
Hallberg, R., 1995: Some aspects of the circulation in ocean basins with isopycnals intersecting the sloping boundaries. Ph.D. thesis, University of Washington, 244 pp.
Hirst, A. C., and T. J. McDougall, 1998: Meridional overturning and dianeutral transport in a *z*-coordinate ocean model including eddy-induced advection. *J. Phys. Oceanogr.,* **28,** 1205–1223.
Holland, W. R., J. C. Chow, and F. O. Bryan, 1998: Application of a third-order upwind scheme in the NCAR ocean model. *J. Climate,* **11,** 1487–1493.
Huang, X., 1998: Mixing and available potential energy in a Boussinesq ocean. *J. Phys. Oceanogr.,* **28,** 669–678.
——, 1999: Mixing and energetics of the oceanic thermohaline circulation. *J. Phys. Oceanogr.,* **29,** 727–746.
Killworth, P. D., and N. R. Edwards, 1997: A turbulent bottom boundary layer code for use in numerical ocean models. *J. Phys. Oceanogr.,* **29,** 1221–1238.
Kunze, E., and T. B. Sandford, 1996: Abyssal mixing: Where it is not. *J. Phys. Oceanogr.,* **26,** 2286–2296.
Large, W. G., J. C. McWilliams, and S. C. Doney, 1994: Oceanic vertical mixing: A review and a model with a nonlocal boundary layer parameterization. *Rev. Geophys.,* **32,** 363–403.
Ledwell, J. R., and A. J. Watson, 1991: The Santa Monica Basin tracer experiment: A study of diapycnal and isopycnal mixing. *J. Geophys. Res.,* **96** (C5), 8695–8718.
——, ——, and C. S. Law, 1993: Evidence for slow mixing across the pycnocline from an open-ocean tracer-release experiment. *Nature,* **364,** 701–703.
Leonard, B. P., 1979: A stable and accurate convective modelling procedure based on quadratic upstream interpolation. *Comput. Methods Appl. Mech. Eng.,* **19,** 59–98.
Levitus, S., 1982: *Climatological Atlas of the World Ocean.* NOAA Professional Paper 13, 173 pp. [Available from the U.S. Government Printing Office, Washington, DC 20402.]
Marotzke, J., 1997: Boundary mixing and the dynamics of three-dimensional thermohaline circulations. *J. Phys. Oceanogr.,* **27,** 1713–1728.
Marshall, J., C. Hill, L. Perelman, and A. Adcroft, 1997: Hydrostatic, quasi-hydrostatic, and nonhydrostatic ocean modeling. *J. Geophys. Res.,* **102,** 5733–5752.
McDougall, T. J., 1987: Thermobaricity, cabbeling, and water-mass conversion. *J. Geophys. Res.,* **92,** 5448–5464.
Molenkamp, C. R., 1968: Accuracy of finite-difference methods applied to the advection equation. *J. Appl. Meteor.,* **7,** 160–167.
Munk, W. H., 1950: On the wind-driven ocean circulation. *J. Meteor.,* **7,** 3–29.
Oberhuber, J. M., 1993: Simulation of the Atlantic circulation with a coupled sea ice-mixed layer-isopycnal general circulation model. Part I: Model description. *J. Phys. Oceanogr.,* **23,** 808–829.
Pacanowski, R. C., and G. Philander, 1981: Parameterization of vertical mixing in numerical models of the tropical ocean. *J. Phys. Oceanogr.,* **11,** 1442–1451.
——, and A. Gnanadesikan, 1998: Transient response in a *z*-level ocean model that resolves topography with partial cells. *Mon. Wea. Rev.,* **126,** 3248–3270.
——, and S. M. Griffies, 1999: *The MOM 3 Manual, Alpha Version.* NOAA/Geophysical Fluid Dynamics Laboratory, 580 pp.
Park, Y.-G., and K. Bryan, 2000: Comparison of thermally driven circulation from a depth coordinate model and an isopycnal layer model. Part I: A scaling law—Sensitivity to vertical diffusivity. *J. Phys. Oceanogr.,* in press.
Pickard, G. L., and W. J. Emery, 1990: *Descriptive Physical Oceanography: An Introduction.* 5th ed. Pergamon Press, 320 pp.
Polzin, K. L., J. M. Toole, J. R. Ledwell, and R. W. Schmidt, 1997: Spatial variability of turbulent mixing in the abyssal ocean. *Science,* **276,** 93–96.
Press, W. H., S. A. Teukolsky, W. T. Vetterling, and B. P. Flannery, 1992: *Numerical Recipes: The Art of Scientific Computing.* 2d ed. Cambridge University Press, 963 pp.
Rhines, P. B., 1977: The dynamics of unsteady currents. *The Sea,* E. D. Goldberg et al., Eds., Vol. 6, Wiley InterScience, 189–318.
Roberts, M., and D. Marshall, 1998: Do we require adiabatic dissipation schemes in eddy-resolving ocean models? *J. Phys. Oceanogr.,* **28,** 2050–2063.
Rooth, C., and G. Östlund, 1972: Penetration of tritium into the Atlantic thermocline. *Deep-Sea Res.,* **19,** 481–492.
Salmon, R., 1998: *Lectures on Geophysical Fluid Dynamics.* Oxford University Press, 378 pp.
Samelson, R. M., and G. K. Vallis: 1997: Large-scale circulation with small diapycnal diffusion: The two-thermocline limit. *J. Mar. Res.,* **55,** 223–275.
Semtner, A. J., and Y. Mintz, 1977: Numerical simulation of the Gulf Stream and mid-ocean eddies. *J. Phys. Oceanogr.,* **7,** 208–230.
Shchepetkin, A. F., and J. C. McWilliams, 1998: Quasi-monotone advection schemes based on explicit locally adaptive dissipation. *Mon. Wea. Rev.,* **126,** 1541–1580.
Stommel, H., 1961: Thermohaline convection with two stable regimes of flow. *Tellus,* **13,** 224–230
Toggweiler, J. R., and B. Samuels, 1998: On the ocean's large-scale circulation near the limit of no vertical mixing. *J. Phys. Oceanogr.,* **28,** 1832–1852.
Toole, J. M., K. L. Polzin, and R. W. Schmidt, 1994: Estimates of diapycnal mixing in the abyssal ocean. *Science,* **264,** 1120–1123.
——, R. W. Schmitt, K. L. Polzin, and E. Kunze, 1997: Near-bound-

ary mixing above the flanks of a midlatitude seamount. *J. Geophys. Res.*, **102** (C1), 947–959.

Treguier, A. M., J. K. Dukowicz, and K. Bryan, 1996: Properties of nonuniform grids used in ocean general circulation models. *J. Geophys. Res.*, **101** (C9), 20 877–20 881.

Veronis, G., 1975: The role of models in tracer studies. *Numerical Models of Ocean Circulation*, National Academy of Sciences.

——, 1977: Use of tracers in circulation studies. *The Sea*, E. D. Goldberg et al., Eds., Vol. 6, Wiley InterScience, 169–188.

Weaver, A. J., and E. S. Sarachik, 1990: On the importance of vertical resolution in certain ocean general circulation models. *J. Phys. Oceanogr.*, **20,** 600–609.

Winters, K. B., and E. A. D'Asaro, 1996: Diascalar flux and the rate of fluid mixing. *J. Fluid. Mech.*, **317,** 179–193.

——, P. N. Lombard, J. J. Riley, and E. A. D'Asaro, 1995: Available potential energy and mixing in density-stratified fluids. *J. Fluid. Mech.*, **289,** 115–128.

Winton, M., R. Hallberg, and A. Gnanadesikan, 1998: Simulation of density-driven frictional downslope flow in *z*-coordinate ocean models. *J. Phys. Oceanogr.*, **28,** 2163–2174.

Zalesak, S. T., 1979: Fully multidimensional flux-corrected transport algorithms for fluids. *J. Comput. Phys.*, **31,** 335–362.